

# Determining Structure-Activity Relationships in Oxide Derived Cu–Sn Catalysts During CO<sub>2</sub> Electroreduction Using X-Ray Spectroscopy

Laura C. Pardo Pérez,\* Alexander Arndt, Sasho Stojkovikj, Ibby Y. Ahmet, Joshua T. Arens, Federico Dattila, Robert Wendt, Ana Guilherme Buzanich, Martin Radtke, Veronica Davies, Katja Höflich, Eike Köhnen, Philipp Tockhorn, Ronny Golnak, Jie Xiao, Götz Schuck, Markus Wollgarten, Núria López, and Matthew T. Mayer\*


The development of earth-abundant catalysts for selective electrochemical CO<sub>2</sub> conversion is a central challenge. Cu–Sn bimetallic catalysts can yield selective CO<sub>2</sub> reduction toward either CO or formate. This study presents oxide-derived Cu–Sn catalysts tunable for either product and seeks to understand the synergetic effects between Cu and Sn causing these selectivity trends. The materials undergo significant transformations under CO<sub>2</sub> reduction conditions, and their dynamic bulk and surface structures are revealed by correlating observations from multiple methods—X-ray absorption spectroscopy for in situ study, and quasi in situ X-ray photoelectron spectroscopy for surface sensitivity. For both types of catalysts, Cu transforms to metallic Cu<sup>0</sup> under reaction conditions. However, the Sn speciation and content differ significantly between the catalyst types: the CO-selective catalysts exhibit a surface Sn content of 13 at. % predominantly present as oxidized Sn, while the formate-selective catalysts display an Sn content of ≈70 at. % consisting of both metallic Sn<sup>0</sup> and Sn oxide species. Density functional theory simulations suggest that Sn<sup>δ+</sup> sites weaken CO adsorption, thereby enhancing CO selectivity, while Sn<sup>0</sup> sites hinder H adsorption and promote formate production. This study reveals the complex dependence of catalyst structure, composition, and speciation with electrochemical bias in bimetallic Cu catalysts.

## 1. Introduction

Copper-based electrocatalysts have been widely studied for CO<sub>2</sub> electrochemical reduction (CO<sub>2</sub>ER) due to their unique capability to produce valuable products such as CO, hydrocarbons, and alcohol. As many as 16 products have been observed during CO<sub>2</sub>ER on polycrystalline Cu.<sup>[1]</sup> The typical major products are formate, CO, ethylene, and methane, minor ones include alcohols and other oxygenates, and the hydrogen evolution reaction (HER) is an (often significant) parasitic reaction. Directing selectivity among this wide variety of products remains a pressing challenge in the field.<sup>[2]</sup> Diverse catalyst engineering approaches to improve the selectivity of Cu have been advanced in the field including the use of nanostructured<sup>[3–6]</sup> as well as oxide-derived Cu catalysts,<sup>[7–12]</sup> as discussed in the comprehensive review by Nitopi et al.<sup>[13]</sup> Another possible approach to modulate

L. C. Pardo Pérez, A. Arndt, S. Stojkovikj, V. Davies, M. T. Mayer  
Young Investigator Group Electrochemical Conversion of CO<sub>2</sub>  
Helmholtz-Zentrum Berlin für Materialien und Energie GmbH  
Hahn-Meitner-Platz 1, 14109 Berlin, Germany  
E-mail: lcpardop@gmail.com; m.mayer@helmholtz-berlin.de

A. Arndt, S. Stojkovikj, V. Davies  
Institut für Chemie & Biochemie  
Freie Universität Berlin  
Arnimallee 22, 14195 Berlin, Germany

 The ORCID identification number(s) for the author(s) of this article can be found under <https://doi.org/10.1002/aenm.202103328>.

© 2021 The Authors. Advanced Energy Materials published by Wiley-VCH GmbH. This is an open access article under the terms of the Creative Commons Attribution License, which permits use, distribution and reproduction in any medium, provided the original work is properly cited.

<sup>[†]</sup>Present address: Ferdi d-Braun-Institut gGmbH, Leibniz-Institut für Höchstfrequenztechnik, 12489 Berlin, Germany

DOI: 10.1002/aenm.202103328

I. Y. Ahmet, R. Wendt, K. Höflich,<sup>[†]</sup> M. Wollgarten  
Institute for Solar Fuels  
Helmholtz-Zentrum Berlin für Materialien und Energie GmbH  
Hahn-Meitner-Platz 1, 14109 Berlin, Germany

J. T. Arens, F. Dattila, N. López  
Institute of Chemical Research of Catalonia (ICIQ)  
The Barcelona Institute of Science and Technology (BIST)  
Av. Països Catalans 16, Tarragona 43007, Spain

A. Guilherme Buzanich, M. Radtke  
Division 6.3 Structure Analysis  
Bundesanstalt für Materialforschung und -prüfung (BAM)  
Richard-Willstätter-Straße 11, 12489 Berlin, Germany

E. Köhnen, P. Tockhorn  
Young Investigator Group Perovskite Tandem Solar Cells  
Helmholtz-Zentrum Berlin für Materialien und Energie GmbH  
Kekuléstraße 5, 12489 Berlin, Germany

R. Golnak, J. Xiao  
Department Highly Sensitive X-ray Spectroscopy  
Helmholtz-Zentrum Berlin für Materialien und Energie GmbH  
Albert-Einstein-Straße 15, 12489 Berlin, Germany

Cu selectivity is to functionalize the Cu surfaces with a second metal to form Cu–M bimetallic catalysts.<sup>[14,15]</sup> In particular, several studies on the CO<sub>2</sub>ER activity of Cu–Sn catalysts have demonstrated remarkably high selectivity towards CO<sup>[16,17]</sup> or formate.<sup>[18,19]</sup> Although a number of empirical trends correlating composition and structure with observed selectivity have been reported, an understanding of the precise mechanistic effects directing selectivity remains elusive.

Comparison of several studies employing various Cu–Sn stoichiometries with similar morphologies<sup>[20–22]</sup> indicates generally that Cu–Sn catalysts with low Sn content are typically selective towards CO production, while those with high Sn content favors formate (HCOO<sup>−</sup>). However, specific optimal compositions leading to high activity towards CO or formate vary significantly among reports. Furthermore, improved activity and selectivity are reported in catalysts with high surface area. Highly CO-selective catalysts have been achieved by the functionalization of high surface area Cu nanostructures with low amounts of Sn by electrodeposition,<sup>[23–25]</sup> electroless deposition,<sup>[26]</sup> or atomic layer deposition (ALD) of SnO<sub>2</sub>.<sup>[16]</sup> Interestingly, high surface area Cu nanostructures functionalized with Sn overlayers have also been reported as highly selective catalysts towards formate.<sup>[19,22,27]</sup> Presumably, significant differences in Cu–Sn surface structure and composition exist among these high surface area catalysts selective toward different products, but unfortunately the detailed analysis of surface composition is rarely reported. Therefore, an investigation of composition and speciation in Sn-functionalized Cu nanostructures tuned to yield radically different selectivity (namely CO or formate) is of high interest to help unravel the factors which direct this selectivity.

Various explanations of the synergetic effects that yield these high selectivities of Cu–Sn bimetallic catalysts have been proposed. According to density functional theory (DFT) investigations, increased HER overpotentials are predicted on Cu–Sn surfaces compared to pure Cu,<sup>[17]</sup> leading to an increased relative selectivity for CO<sub>2</sub>ER over HER on Cu–Sn materials. As for the possible effects of Cu–Sn composition directing selectivity among CO or formate pathways, Vasileff<sup>[28]</sup> reported a Bader charge analysis indicating a partial electron transfer (ET) from Sn to Cu in CuSn alloys, leading to the formation of partially oxidized Sn<sup>δ+</sup> sites and partially reduced Cu<sup>δ−</sup> sites. This partial ET is proposed to gradually weaken the adsorption of \*COOH (leading to CO) with increasing Sn content and enhance \*OCHO adsorption (leading to HCOO<sup>−</sup>). Meanwhile, the persistence of oxidized Sn as an active site during CO<sub>2</sub>ER experiments has been invoked by Li et al. based on DFT studies,<sup>[22]</sup> who proposed that Cu-doped uniaxially-compressed SnO<sub>2</sub> is the active site for selective reduction of CO<sub>2</sub> to CO in Cu@SnO<sub>2</sub> (core@shell) nanoparticle catalysts.

These DFT studies on Cu–Sn bimetallic CO<sub>2</sub>ER catalysts indicate that charge distribution among metal sites and their oxidation states play a crucial role in the binding strength of the key intermediates directing selectivity between H<sub>2</sub>, CO, and formate. At the center of the debate is the possible persistence of oxidized metal sites under CO<sub>2</sub>ER reduction conditions and

the precise nature of the active site. While these DFT models are typically based on compositions observed either before or after electrocatalyst testing, it is well known that electrocatalyst materials can transform significantly under CO<sub>2</sub> reduction conditions, presenting challenges in identifying their actual active forms. In this context, the complementary techniques of X-ray absorption (XAS) and X-ray photoelectron (XPS) spectroscopy are powerful techniques to probe the chemical environment and oxidation state of Cu and Sn and gather relevant information on the active form of the catalysts.

Herein, we present an X-ray spectroscopy study of a Cu–Sn bimetallic system with tunable Sn content capable of achieving high selectivity to either CO or formate. Complementary information on the composition and chemical environment of metals in the electrocatalysts' bulk and surface was revealed by correlating observations from multiple X-ray spectroscopy methods (in situ hard-XAS, ex situ soft-XAS, and quasi in situ XPS). Finally, DFT simulations unveil the role of Sn speciation in driving CO and HCOO<sup>−</sup> selectivity. Our study reveals a complex correlation between catalyst structure, composition, and speciation with applied electrochemical bias in Sn-functionalized Cu catalysts.

## 2. Results & Discussion

### 2.1. Material Synthesis & Characterization

The preparation of nanostructured Cu–Sn electrocatalysts was adapted from the method reported by Schreier et al.<sup>[16]</sup> Complete experimental details are provided in Section S1, Supporting Information. In a first step, electrodes based on arrays of Cu(OH)<sub>2</sub> nanowires, denoted hereafter CuNW, were synthesized by anodization of Cu films (1 μm) sputter deposited on glass substrates. The anodization was carried out at a constant current of 8 mA cm<sup>−2</sup> to reach a total charge of 1.35 C cm<sup>−2</sup> and the samples were subsequently annealed in air at 150 °C for 1 h (Figure 1a). This procedure yields reproducible bundled nanowire arrays with lengths of several μm (≈8–10 μm) and diameters of hundreds of nm (200–400 nm), which are attached to a continuous Cu base layer, as seen in Figure 1b–d.

The so-obtained Cu(OH)<sub>2</sub> nanowires were then modified by ultrathin SnO<sub>2</sub> layers generated by ALD with varied number of deposition cycles, denoted hereafter CuNW-SnXc (Xc = X number of ALD cycles). The ALD method allows uniform and conformal coating of the high surface area nanostructures with SnO<sub>2</sub>, and variation of the deposition cycles enables us to precisely modulate the surface Sn content, while avoiding significant changes in morphology (Figure 1 and Figure S1, Supporting Information). The number of deposition cycles was varied across the range 1–182, which correspond to expected nominal thicknesses of approximately 0.1–20 nm based on calibrated deposition rates. The X-ray diffraction (XRD) patterns of the samples modified with 15 and 182 ALD cycles of SnO<sub>2</sub> display the typical pattern for CuO (Figure 1e), indicating that the Cu(OH)<sub>2</sub> nanowires are dehydrated under the ALD conditions (120 °C under vacuum). Note that the observed Cu<sup>0</sup> metallic diffraction peaks arise from the underlying residual sputtered Cu, as can be seen in the cross-section scanning electron microscopy (SEM) micrograph (Figure 1d). This continuous Cu layer—a result of only partially anodizing the original film—is

G. Schuck  
Department Structure and Dynamics of Energy Materials  
Helmholtz-Zentrum Berlin für Materialien und Energie GmbH  
Hahn-Meitner-Platz 1, 14109 Berlin, Germany

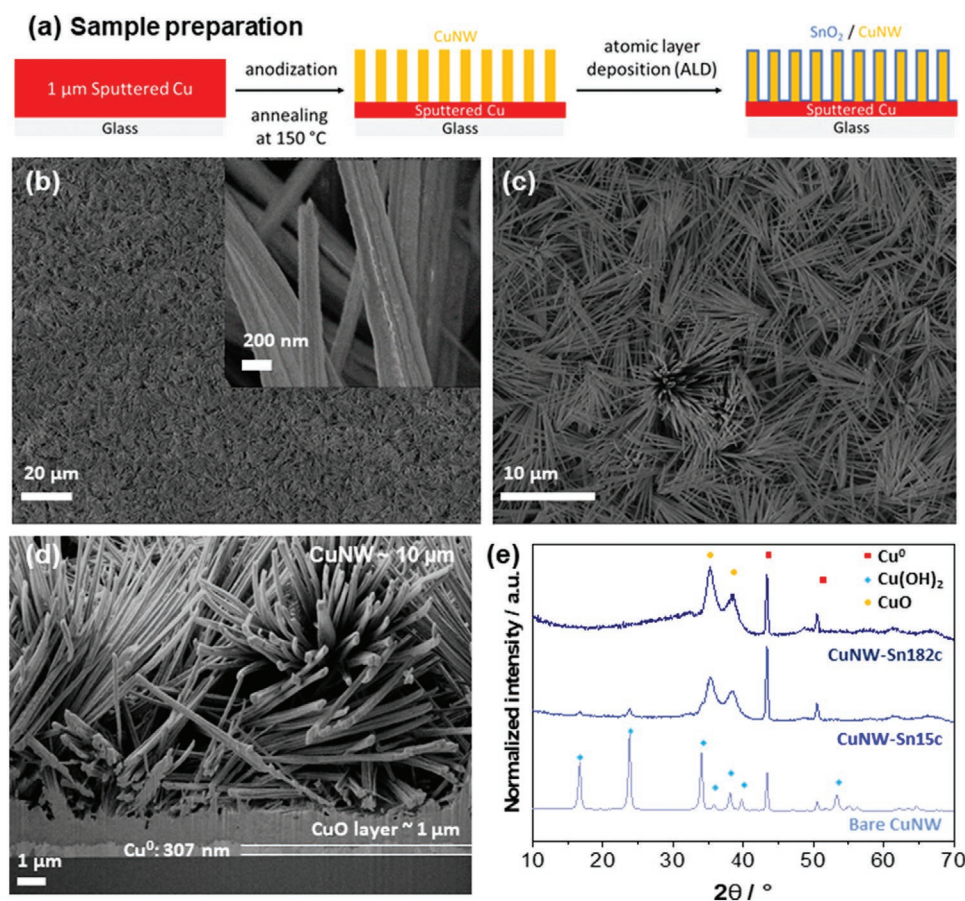


**Figure 1.** a) Schematic of synthesis procedure. b,c) SEM micrographs of the AS CuNW modified with 15 cycles of ALD  $\text{SnO}_2$ . d) Cross-section SEM micrograph of CuNW-Sn15c at the site of a Focused Ion Beam cut. e) Grazing incidence XRD patterns of AS CuNW bare and modified with 15 or 182 cycles of  $\text{SnO}_2$  ALD.

important for maintaining the integrity and conductivity of the NW arrays as a functioning electrode. As seen in Figure 1d, a compact  $\text{CuO}$  layer above it likely prevents the metallic underlayer from contributing to the electrocatalysis.

The samples were tested for  $\text{CO}_2$  electroreduction in  $\text{CO}_2$  saturated 0.1 M  $\text{KHCO}_3$  in a custom-made three-electrode two-compartment cell separated by a Nafion 115 membrane, under a constant flow of  $\text{CO}_2$ . Since the CuNW-SnXc was originally composed of  $\text{Cu}(\text{OH})_2$  (bare CuNW) or  $\text{CuO}$  ( $\text{SnO}_2$  ALD modified samples) and variable amounts of  $\text{SnO}_2$ , the oxide composites were pre-reduced by chronopotentiometry (CP) at a constant current of  $-2 \text{ mA cm}^{-2}$  to reach a potential of  $-0.5 \text{ V}$  versus RHE (reversible hydrogen electrode; all potentials reported hereafter are referred to RHE unless otherwise specified). Directly after the pre-reduction step, the samples were set at the desired  $\text{CO}_2$  electrolysis potential, typically  $-0.7 \text{ V}$  where the maximum efficiency for CO has been reported for this system.<sup>[16]</sup> Representative pre-reduction CP and chronoamperometry data are presented in Figure S2, Supporting Information. The  $\text{CO}_2$ ER activity at  $-0.7 \text{ V}$  for samples modified with various numbers of  $\text{SnO}_2$  ALD cycles (between 1–182) is displayed as faradaic efficiency and partial current densities in Figure 2a,b. The results show that modifying the CuNW with a single cycle of  $\text{SnO}_2$  induces a significant shift in selectivity, namely the near-complete suppression of formate and a large increase in CO

selectivity. Increasing the  $\text{SnO}_2$  to 15 cycles further improves CO selectivity over  $\text{H}_2$  and ethylene, reaching an optimal faradaic efficiency together with the highest CO partial current density (Figure 2b). Further increasing  $\text{SnO}_2$  to 20, 25, and 182 cycles ( $\approx 20 \text{ nm}$ ) induces a decrease in CO selectivity and production rate, as well as total current density. Such volcano-type behavior was previously reported by Schreier et al.<sup>[16]</sup> albeit with different optimal numbers of  $\text{SnO}_2$  ALD cycles, presumably due to the use of different ALD system conditions. As noted above, the  $\text{Cu}(\text{OH})_2$  dehydrates to  $\text{CuO}$  during the ALD process. We performed a series of control experiments, pre-dehydrating  $\text{Cu}(\text{OH})_2$  to  $\text{CuO}$  before ALD (Figure S3, Supporting Information). The results indicate that the dehydration of  $\text{Cu}(\text{OH})_2$  to  $\text{CuO}$  itself induces only minor changes in  $\text{CO}_2$ ER selectivity, whereas after the addition of 15 ALD cycles of  $\text{SnO}_2$  to each, the Sn-functionalized  $\text{Cu}(\text{OH})_2$  and  $\text{CuO}$  nanowire samples both obtained high CO faradaic efficiency (79% and 83% respectively).

The CuNW modified with 15 ALD cycles, hereafter denoted CuNW-Sn<sub>LOW</sub>, displays the optimal composition for CO production with the highest faradaic selectivity (79%) and CO partial current density of  $\approx -2.5 \text{ mA cm}^{-2}$ . Its  $\text{CO}_2$ ER performance was further investigated in the potential range from  $-0.5$  to  $-0.9 \text{ V}$  (Figure 2c). This composite displays high CO selectivity across the moderate overpotential range  $-0.6$  to  $-0.8 \text{ V}$ , decreasing at lower and higher potentials in favor of increased hydrogen



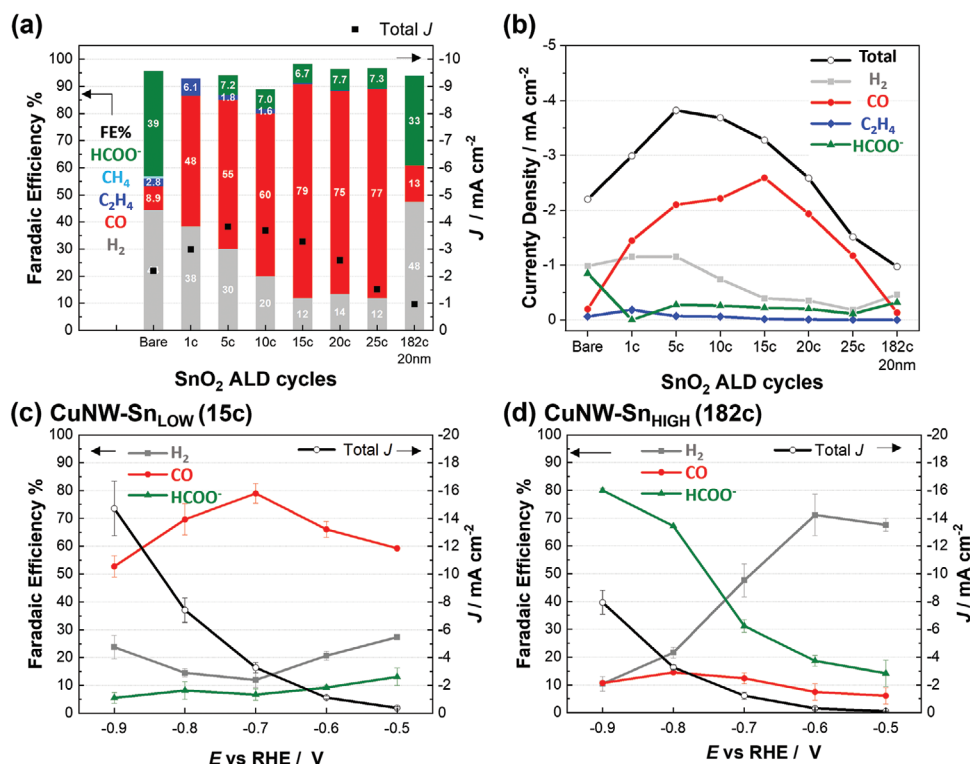


**Figure 2.** CO<sub>2</sub>ER activity for different CuNW samples modified with various numbers of SnO<sub>2</sub> ALD cycles, each tested at  $-0.7$  V versus RHE in  $0.1$  M KHCO<sub>3</sub>. a) Faradaic efficiencies and b) partial current densities. CO<sub>2</sub>ER as a function of applied potential for c) CuNW-Sn<sub>15c</sub> and d) CuNW-Sn<sub>182c</sub>. Error bars correspond to standard deviation of at least three independent samples tested at each potential.

evolution. Low formate selectivity is observed across the examined range. Therefore, this addition of an ultrathin ALD layer of SnO<sub>2</sub> (15 cycles correspond to a nominal thickness  $\approx 1.6$  nm) results in a significant alteration of product selectivity toward CO, as compared to the mixture of several products observed on bare CuNW (CO<sub>2</sub>ER activity shown in Figure S4, Supporting Information). The observation that this intermediate loading of SnO<sub>2</sub> produced the best selectivity and rate for CO formation suggests that there is an important synergy between Cu and Sn which is responsible for this optimized activity.

The CuNW modified with a high SnO<sub>2</sub> content (182 ALD cycles, corresponding to a nominal film thickness of approx. 20 nm), hereafter denoted CuNW-Sn<sub>HIGH</sub>, was also investigated across the same potential range (Figure 2d). Although at  $-0.7$  V this catalyst produced a mix of products dominated by H<sub>2</sub>, at more negative potentials the selectivity to hydrogen greatly decreases while formate increases significantly to become the primary product (FE 80% at  $-0.9$  V). Meanwhile, the CO selectivity for this composite remains low at all tested potentials. Thus, at sufficiently high loading of Sn, the composite samples exhibit high formate selectivity comparable to what has been reported for pure Sn catalysts.<sup>[29–31]</sup>

Scanning electron microscopy (SEM) characterization of the catalysts after CO<sub>2</sub> electrolysis is presented in Figure S5, Supporting Information. The materials display mostly preserved nanowire structures with roughened surfaces. Energy-dispersive X-ray spectroscopy (EDX) quantification of bulk composition (Table 1, Figures S6 and S7, Supporting Information) shows that a decreased Sn content is observed after electrolysis experiments; in CuNW-Sn<sub>LOW</sub> the bulk Sn fraction (referred to total metal Sn+Cu) decreases from  $2.2 \pm 0.3$  at. % in the as-

synthesized (AS) catalyst to  $1.9 \pm 0.2$  at. % after electrolysis at  $-0.9$  V. In the case of CuNW-Sn<sub>HIGH</sub> the Sn content decreases from  $23 \pm 1.1$  at. % in the AS catalyst to  $16 \pm 1.3$  at. % after electrolysis at  $-0.9$  V. Partial dissolution of Sn was further confirmed by inductively coupled plasma-optical emission spectrometry (ICP-OES) analysis of electrolyte (Table S1, Supporting Information). Together these results demonstrate that the SnO<sub>2</sub> ALD modification of CuNW electrodes enables the modulation of the Cu–Sn bimetallic composition to reach high selectivity toward either CO in CuNW-Sn<sub>LOW</sub> or formate in CuNW-Sn<sub>HIGH</sub> with minor changes to the nanoscale morphology of the electrodes (Figure S1 and Section S5, Supporting Information).

These two composites were selected as CO- and formate-selective Cu–Sn catalysts for further investigation of synergetic effects between metals through correlation of observations gathered by different X-ray spectroscopy methods (in situ hard-XAS, ex situ soft-XAS, and quasi in situ XPS). Complimentary information on oxidation states and chemical environment of Cu and Sn in CuNW-Sn electrocatalysts' bulk and surface following progressive electroreduction stages has been assessed to gather relevant information on the active form of the catalysts. The X-ray spectroscopy observations and their correlation with CO<sub>2</sub>ER activity trends are discussed in the following sections.

## 2.2. In Situ Investigation of Cu and Sn K-Edges during CO<sub>2</sub>ER via Hard X-Ray Absorption Spectroscopy

The Cu K-edge XAS measurements were conducted at the KMC-2 beamline at the BESSY II synchrotron.<sup>[32]</sup> The

**Table 1.** Summary of bulk and surface characterization XRD, EDX, and XPS for CuNW modified with low and high Sn content by ALD overlayers AS and following CO<sub>2</sub> reduction at different applied potentials.

Sample description		CO <sub>2</sub> ER Main product (FE)	Bulk structure XRD/Hard XAS	Sn at. % <sup>a),b)</sup>		Surface speciation
				Bulk (SEM-EDX)	Surface (XPS)	
CuNW-Sn <sub>LOW</sub>	as-synthesized		CuO	2.2 ± 0.3	24 ± 4.9	CuO/SnO <sub>x</sub>
	−0.5 V	CO (60%)	Cu <sup>0</sup>		19 ± 1.9	Cu <sup>0</sup> /SnO <sub>x</sub>
	−0.7 V	CO (79%)	Cu <sup>0</sup>	1.5 ± 0.1	13 ± 0.7 (14 ± 0.8) <sup>c)</sup>	Cu <sup>0</sup> /SnO <sub>x</sub>
	−0.9 V	CO (53%)	Cu <sup>0</sup>	1.9 ± 0.2	14 ± 0.3 (14 ± 3.8) <sup>c)</sup>	Cu <sup>0</sup> /SnO <sub>x</sub>
CuNW-Sn <sub>HIGH</sub>	as-synthesized		CuO	23 ± 1.1	100 ± 0	CuO/SnO <sub>x</sub>
	−0.5 V	H <sub>2</sub> (67%)	Cu <sup>0</sup>		98 ± 0.4	Cu <sup>0</sup> /SnO <sub>x</sub>
	−0.6 V	H <sub>2</sub> (71%)	Cu <sup>0</sup>		93 ± 1.5	Cu <sup>0</sup> /SnO <sub>x</sub>
	−0.7 V	Formate (67%)	Cu <sup>0</sup> /Cu <sub>6</sub> Sn <sub>5</sub>	17 ± 2.6	78 ± 0.2 (82 ± 1.4) <sup>c)</sup>	Cu <sup>0</sup> /Sn <sup>0</sup> /SnO <sub>x</sub>
	−0.9 V	Formate (80%)	Cu <sup>0</sup> /Cu <sub>6</sub> Sn <sub>5</sub>	16 ± 1.3	70 ± 2.3 (77 ± 2.1) <sup>c)</sup>	Cu <sup>0</sup> /Sn <sup>0</sup> /SnO <sub>x</sub>

<sup>a)</sup>Sn at. % relative to total metal (Cu+Sn); <sup>b)</sup>Sn at. % data presented as the average value ± standard deviation at 3 different sample locations; <sup>c)</sup>Sn at. % after intentional exposure of samples to air for 20 min

penetration length of X-ray photons through matter is a function of their energy and the phases through which they pass, with higher energy photons capable of traveling further through condensed matter without complete attenuation. This enables the use of high-energy “hard” X-rays for in situ studies of electrode materials in operating electrochemical cells. Photons with energy corresponding to the Cu K-edge (located at 8979 eV) have an approximate probing depth of ≈4 μm in Cu and ≈1.4 mm in water.<sup>[33,34]</sup> A custom electrochemical cell with a polymer window and a thin electrolyte layer of ≈500 μm (CO<sub>2</sub> sat. 0.1 M KHCO<sub>3</sub>) was fabricated to enable hard X-ray absorption measurements of the electrode in fluorescence detection mode, under electrochemical CO<sub>2</sub>ER conditions. The cell and spectroscopy setup employed for these measurements are shown in Figure S9, Supporting Information. Considering that the CuNW arrays atop the glass substrate exhibit a porous structure with thickness in the μm range (see Figure 1 b–d), it is expected that the incoming radiation probes the bulk of CuNW and the underlying sputtered Cu as well, as will be discussed later. According to FIB cross-section images the samples have an underlying sputtered Cu<sup>0</sup> layer of 300–400 nm thickness (Figure 1d and Figure S1, Supporting Information).

The CuNW samples modified with different amounts of SnO<sub>2</sub> were investigated in their AS state as well as in situ during both the CP pre-reduction step and CO<sub>2</sub> electrolysis. The Cu K-edge X-ray Absorption Near-Edge Structure (XANES) spectra and Fourier Transform Extended X-ray Absorption Fine Structure (FT-EXAFS) analyses are shown in Figure 3. In the AS state the bare CuNW electrode displays a XANES spectrum typical of Cu(OH)<sub>2</sub> (Figure 3c). In samples CuNW-Sn<sub>LOW</sub> and CuNW-Sn<sub>HIGH</sub> the spectra resemble the standard CuO spectrum as indicated by the shoulder ≈8982 eV, presumably due to dehydration of Cu(OH)<sub>2</sub> to CuO under ALD conditions (120 °C under vacuum, see experimental details in the Supp. Info.) in agreement with the diffraction patterns (Figure 1e). Additionally, all AS samples exhibit an early shoulder at ≈8977 eV attributable to the sputtered metallic Cu<sup>0</sup> layer below the CuNW (Figure 1d). The k<sub>2</sub>-weighted FT-EXAFS analysis of AS samples

Cu K-edge spectra are displayed in Figure 3d. The peak 1.6 Å corresponds to the Cu–O distance in both CuO and Cu(OH)<sub>2</sub>, while the peak at 2.3 Å corresponds to the Cu–Cu distance in the underlying sputtered metallic Cu layer, in agreement with previous reports.<sup>[35,36]</sup>

With the aim of investigating possible effects of Sn content on the progressive reduction of Cu, several Cu K-edge XANES spectra (each acquired for ≈20 min) were collected during chronopotentiometric (CP) pre-reduction of bare CuNW as well as samples CuNW-Sn<sub>LOW</sub> and CuNW-Sn<sub>HIGH</sub>. Although under standard conditions this pre-reduction step was typically carried out at −2 mA cm<sup>−2</sup>, taking on average 8–10 min (see Figure S2, Supporting Information), here the activation was carried out at a lower current density of −0.2 mA cm<sup>−2</sup> in order to allow sufficient time to collect a series of XANES spectra at different stages during the activation step. These spectra are shown in Figure 3a, color-coded to match the CP time frame in which they were collected (Figure 3b). For all types of samples, with or without Sn deposited, the experiments show the progressive transition from Cu<sup>2+</sup> to Cu<sup>0</sup> that completes after about 70 min of CP pre-reduction. The results indicate that roughly the same amount of charge has been passed on all samples at the point where defined XANES Cu<sup>0</sup> features are observed; this signifies that about the same amount of Cu<sup>2+</sup> has been reduced in each case, although more reductive potentials are required for reduction of samples containing Sn (Figure 3b and Figure S2, Supporting Information).

After CP pre-reduction until reaching a potential of −0.4 V, the samples were held at this potential for 30 min for collection of additional XANES spectra (see Figure S10, Supporting Information). However, at this stage the samples transition from self-reduction to electrocatalytic CO<sub>2</sub>ER and HER, and bubble formation due to the formation of gaseous products commences, causing disruptions to the measurement of a stable signal. To perform EXAFS data collection, a longer collection time in the post edge region is necessary, requiring a very stable signal over a duration of ca. 2.5 h per spectrum. Thus, to allow EXAFS collection, the reduction bias was decreased to −0.1 V, a potential sufficiently reducing to observe a sustained

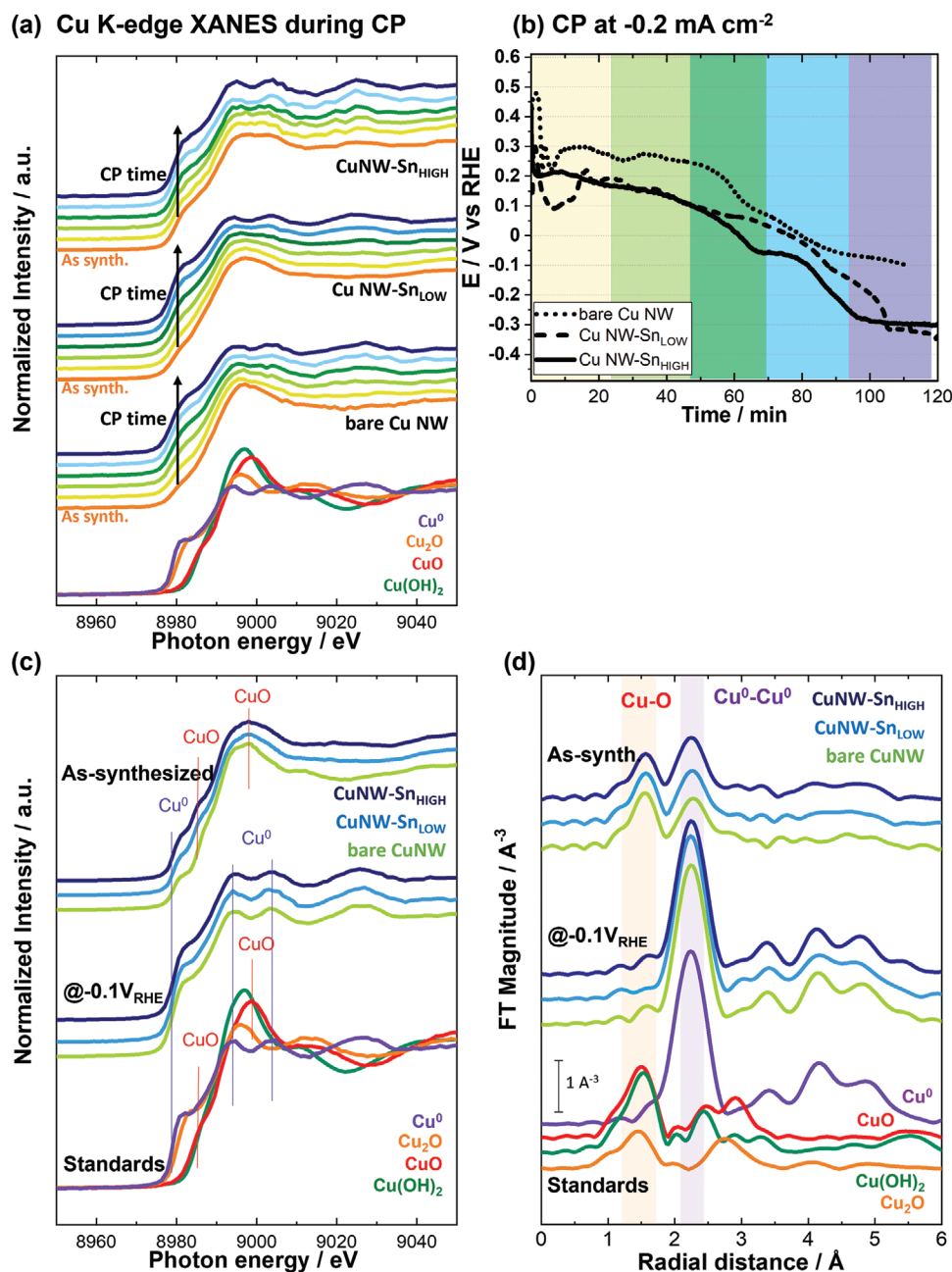


**Figure 3.** In situ Cu K-edge XAS investigation of CuNW electrodes modified with variable number of SnO<sub>2</sub> ALD cycles. a) XANES spectra collected during CP activation, b) CP activation at  $-0.2 \text{ mA cm}^{-2}$ . The spectra in (a) are color-coded to match the CP time frame (b) in which they were collected. Cu K-edge spectra, c) Cu K-edge XANES spectra collected in the AS state and during CO<sub>2</sub>ER at  $-0.1 \text{ V}$ , and d) corresponding k<sub>2</sub>-weighted FT-EXAFS in the k range between 3–12 (note displayed FT-EXAFS is not phase corrected). Reference spectra collected from standards of metallic Cu<sup>0</sup>, CuO, Cu(OH)<sub>2</sub>, and Cu<sub>2</sub>O are presented for comparison.

catalytic reduction current ( $\approx 150\text{--}200 \text{ } \mu\text{A cm}^{-2}$ ) without observable bubble-induced noise. The resulting Cu K-edge XANES spectra at  $-0.1 \text{ V}$  are shown in Figure 3c; all the samples exhibit the typical features of metallic Cu<sup>0</sup> characterized by an early shoulder  $\approx 8977 \text{ eV}$ , and all show a dominant EXAFS peak at  $2.3 \text{ Å}$  (Figure 3d) attributable to the Cu–Cu distance in metallic Cu<sup>0</sup> during CO<sub>2</sub>ER turnover. No significant differences were observed between the XANES spectra collected at  $-0.4$  or  $-0.1 \text{ V}$  versus RHE—for both conditions, all samples

have spectra closely matching that of metallic Cu<sup>0</sup>, as shown in Figure S10, Supporting Information.

These results are in good agreement with ex situ GI-XRD characterization (Figure S8, Supporting Information): after electrolysis CuNW-Sn<sub>LOW</sub> displays the diffraction pattern of metallic Cu<sup>0</sup>, while CuNW-Sn<sub>HIGH</sub> shows a mix of Cu<sup>0</sup> and Cu<sub>6</sub>Sn<sub>5</sub> alloy. These observations indicate that the bulk of the CuNW samples is reduced under CO<sub>2</sub>ER catalytic conditions and the use of hard X-rays enabled the observation of the

dynamic transformation of reduction of Cu. Note that Cu–Sn and Cu–Cu distances in  $\text{Cu}_6\text{Sn}_5$  and metallic Cu are very close ( $\approx 2.3$  Å without phase correction)<sup>[18,36]</sup> and are not distinguishable from each other in EXAFS analysis. However, as will be discussed below, the transmission electron microscopy (TEM) investigation of CuNW-Sn<sub>HIGH</sub> (Figure 6 and Figure S15, Supporting Information) provided further evidence of the formation of  $\text{Cu}_6\text{Sn}_5$  during  $\text{CO}_2$  electrolysis.

The Sn speciation during  $\text{CO}_2$ ER was investigated by in situ XANES at the Sn K-edge (with hard X-ray energies ca. 29.2 keV), conducted at the BAMline at BESSY II.<sup>[37]</sup> The experimental details can be found in Section S3.2, Supporting Information. Both sample types in the AS condition showed the typical features of  $\text{SnO}_2$ . CuNW-Sn<sub>HIGH</sub> was further investigated during  $\text{CO}_2$ ER at increasingly negative bias between  $-0.5$  and  $-0.9$  V, which led to a progressive decrease in the relative amplitude of the white line peak prominent in the oxides  $\text{SnO}_2$  and  $\text{SnO}$ , indicating the growth of a metallic Sn component (Figure S12a, Supporting Information). Linear combination fitting analysis of the XANES spectra (Figure S12c, Supporting Information) indicates that at  $-0.5$  and  $-0.6$  V the  $\text{SnO}_2$  oxide is partially reduced to  $\text{SnO}$  and a minor amount of  $\text{Sn}^0$  ( $< 6\%$  at  $-0.6$  V), at  $-0.7$  V and  $-0.9$  V the  $\text{Sn}^0$  component grows with increasingly reductive bias (to 72% at  $-0.9$  V), and  $\text{SnO}_2$  is observed to persist at all tested potentials.

In the case of CuNW-Sn<sub>LOW</sub>, XANES spectra collected at  $-0.5$  and  $-0.7$  V also display a partial flattening of the  $\text{SnO}_2$  white line feature, indicative of partial reduction of  $\text{SnO}_2$  (Figure S12b, Supporting Information). However, the low Sn content leads to a low signal-to-noise ratio, hindering further quantitative analysis of the data. Nevertheless, the persistence of the white line feature in the spectra collected during  $\text{CO}_2$ ER at  $-0.5$  and  $-0.7$  V indicates that Sn is (at least partially) present in an oxidized state.

Overall, the in situ XAS investigation of Cu and Sn K-edges revealed dynamic potential-dependent transformations of both elements in the CuNW-Sn electrocatalysts under  $\text{CO}_2$  electroreduction conditions. For Cu, the bulk reduction of  $\text{CuO}$  NW to  $\text{Cu}^0$  in all CuNW-Sn samples (regardless of Sn content) is verified during CP activation at potentials as mild as  $-0.4$  V versus RHE. In contrast, CuNW-Sn<sub>HIGH</sub> and CuNW-Sn<sub>LOW</sub> samples both displayed partial reduction of the  $\text{SnO}_2$  layer into metallic  $\text{Sn}^0$  while retaining features of persistent oxidized Sn at potentials as reductive as  $-0.7$  and  $-0.9$  V.

Given the bulk sensitivity of the XAS measurements conducted using hard X-rays, the possibility of persistent surface or subsurface copper oxide (as reported in some previous studies on pure Cu catalysts)<sup>[38,39]</sup> could not be adequately investigated by this method. To more selectively probe the catalysts' surfaces, complimentary investigations by soft X-ray XAS and XPS were conducted, as discussed in the following sections.

### 2.3. Investigation of Surface Composition via Ex Situ Soft XAS and Quasi In Situ XPS

The electrode surface composition was initially investigated by ex situ XAS, using the LiXEdrom experimental station at the UE56/2 PGM-2 beamline at BESSY II.<sup>[40]</sup> The Cu L- and Sn M-edge spectra were investigated in the soft X-ray range using total electron yield (TEY) detection mode, whereby the probing

depth is less than 10 nm, limited by the mean free path of generated photoelectrons.<sup>[41,42]</sup> While this method offers good surface sensitivity, the attenuation of soft X-rays and photoelectrons in water prevents this method from being applied in situ during electrocatalysis. To achieve surface-sensitive analysis of samples resembling their catalytically-active form, we compromised by first conducting the electrochemical experiments (CP pre-reduction until  $-0.5$  V, and electrolysis a constant potential of  $-0.7$  V) inside an  $\text{O}_2$ -free glovebox and then transferring them directly into the high-vacuum chamber for soft XAS analysis, thus mitigating electrode re-oxidation in air, although a brief period of air exposure ( $\approx 15$ – $20$  min) was unavoidable during the transfer step. CuNW samples and a series of relevant standards (Cu and Sn metals and oxides) were measured. The results are presented in Section S3.3 and Figure S13, Supporting Information).

The soft X-ray absorption investigation provides insight on the surface structure and composition changes taking place in the CuNW-Sn samples during  $\text{CO}_2$  electroreduction. In all samples, surface Cu appears readily reduced from  $\text{Cu}^{2+}$  to  $\text{Cu}^0/\text{Cu}^+$  after the pre-reduction step to  $-0.5$  V (Figure S13a, Supporting Information). On the other hand, Sn persists as a  $\text{SnO}_x$  enriched surface overlayer after the pre-reduction step (Figure S13b, Supporting Information). However, after electrolysis at  $-0.7$  V, the Sn M-edge signal decreases for both samples CuNW-Sn<sub>LOW</sub> and CuNW-Sn<sub>HIGH</sub> in comparison to the AS state, indicating a significant decrease in Sn content at the near-surface depth ( $< 10$  nm) probed by soft XAS, presumably due to migration from surface to bulk or dissolution. Additionally, the results indicate residual surface content of oxidized Cu as  $\text{Cu}^+$  and  $\text{Cu}^{2+}$ , as well as  $\text{SnO}$ . Due to the surface-sensitive nature of this ex situ method and the unavoidable air exposure which likely induced some degree of surface oxidation, we cannot be certain whether the observed  $\text{Cu}^+$ ,  $\text{Cu}^{2+}$ , and  $\text{SnO}$  surface species persisted under  $\text{CO}_2$ ER conditions or if they were formed spontaneously by oxidation in air. Nevertheless, a reproducible trend of  $\text{Cu}^{2+}$  signal in CuNW-Sn<sub>LOW</sub> sample in the different conditions tested suggests that the presence of low amounts of Sn may render near-surface Cu atoms more prone to oxidation, in contrast to the Sn-free bare CuNW sample which is free of  $\text{Cu}^{2+}$  signal after  $\text{CO}_2$ ER. Similar trends were observed in ex situ surface-sensitive XPS investigations of CuSn alloys.<sup>[20,21]</sup>

In order to investigate if the copper and tin oxidized species observed by ex situ soft XAS (Figure S13a,b, Supporting Information) are the product of fast reoxidation during brief air exposure and quantify the observed decrease of surface Sn during catalytic turnover, a quasi in situ investigation by XPS was conducted.<sup>[43]</sup> XPS spectra for CuNW samples with different  $\text{SnO}_x$  content (bare CuNW, CuNW-Sn<sub>LOW</sub>, and CuNW-Sn<sub>HIGH</sub>) were collected in AS condition as well progressive reductive conditions after CP pre-reduction to  $-0.5$  V, after 2 h catalysis at  $-0.7$  V, and after 2 h catalysis at  $-0.9$  V. The electrochemical testing was conducted under inert atmosphere in a glovebox, then the samples were dried, and promptly transferred to the XPS chamber using a gastight transfer module. By this method, the exclusion of atmospheric oxygen exposure is ensured, preventing oxidation and making the resulting electrode surfaces more representative of their active forms, while also taking advantage of the surface sensitivity of XPS.



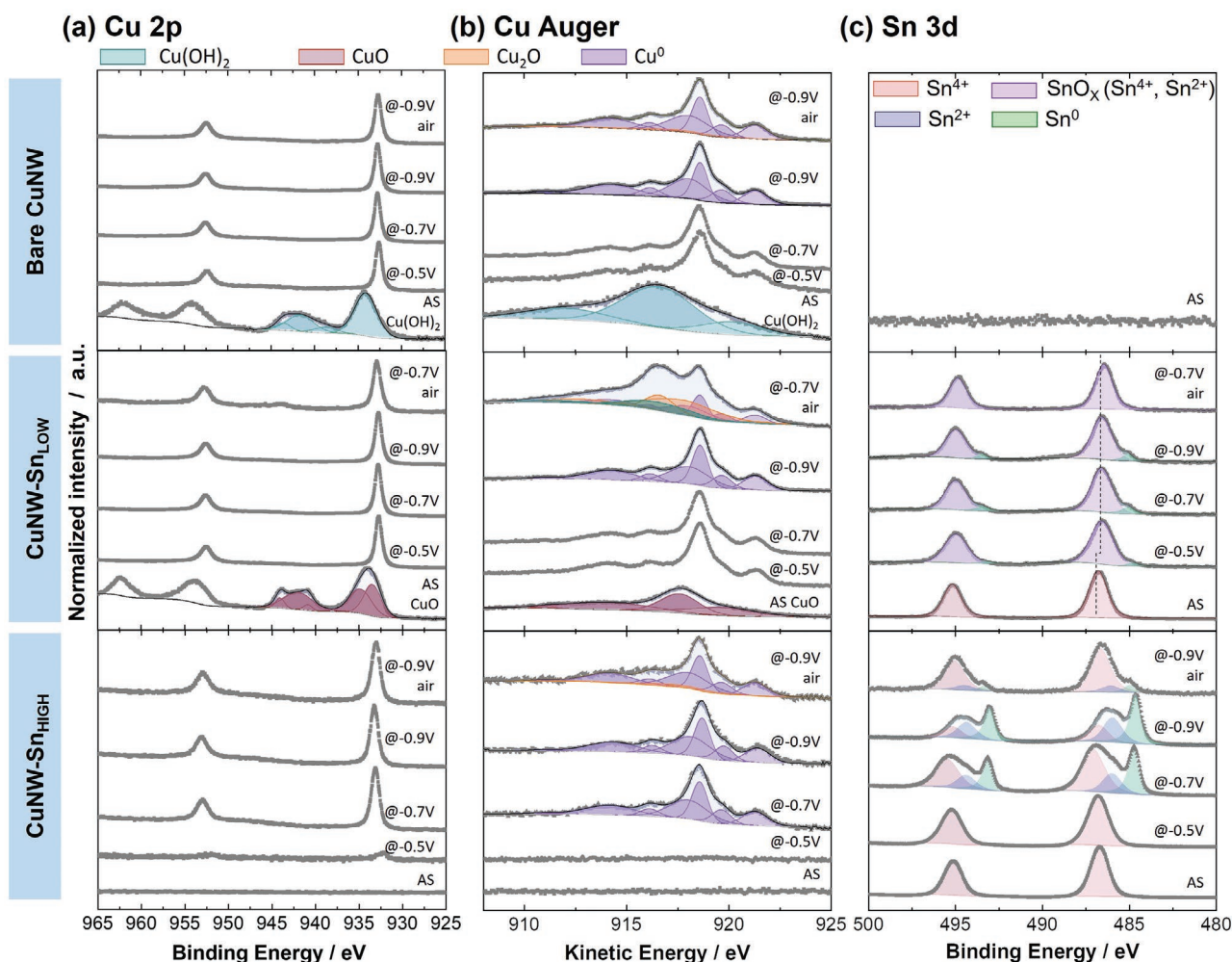


**Figure 4.** XPS spectra for a) Cu 2p, b) Cu Auger, and c) Sn 3d core levels for CuNW samples modified with different SnO<sub>2</sub> content (bare CuNW (top), CuNW-Sn<sub>LOW</sub> (middle), and CuNW-Sn<sub>HIGH</sub> (bottom)) in their AS state and after different electrochemical tests: after CP activation at  $-2 \text{ mA cm}^{-2}$  up to  $-0.5 \text{ V}$ , after 2 h CO<sub>2</sub>ER at  $-0.7$  and  $-0.9 \text{ V}$ , and after exposure to air. Spectra are presented with a vertical offset to facilitate comparison. Electrochemical tests were conducted in an inert gas glovebox at the specified potential for 2 h followed by removal from the electrolyte and transfer to the XPS chamber without air exposure.

The AS samples display the expected spectral features (Figure 4). In agreement with the XRD characterization bare CuNW displays a Cu 2p spectrum (main peak at binding energy (BE) of 933.9 eV and shake-up satellite structure) and Cu LMM Auger spectrum typical for Cu(OH)<sub>2</sub>. The sample modified with a low content of Sn, CuNW-Sn<sub>LOW</sub>, exhibits Cu 2p (main peak at BE 934.1 eV and shake-up satellite structure) and Cu LMM spectral features of CuO. For both samples, Cu 2p and Cu LMM Auger spectra can be accurately fitted with the peak model described by Biesinger et al.<sup>[44]</sup> for Cu(OH)<sub>2</sub> and CuO (see details on peak model in Section S4.1, Table S3, Supporting Information).

The study of progressive reduction on the bare CuNW sample indicates that the catalysts' surfaces are fully reduced to metallic Cu<sup>0</sup> after CP activation up to  $-0.5 \text{ V}$  (Figure 4a,b) as indicated by the sharp Cu 2p doublet with the main peak at BE 932.7 eV, as well as the metallic Cu<sup>0</sup> Cu LMM Auger fingerprint characterized by a multiplet centered at a sharp main peak at a kinetic energy (KE) of 918.6 eV. The Cu LMM spectra can be evaluated

by the peak model described by Biesinger et al. for freshly sputtered metallic Cu surface and validated by an additional internal reference measurement of an Ar sputtered Cu foil (see details on peak model in Section S4.1, Table S2, Supporting Information). Similar Cu 2p and Cu LMM spectra are observed for samples after CO<sub>2</sub> electrolysis at  $-0.7$  and  $-0.9 \text{ V}$ , indicating that Cu is fully reduced at the surface to metallic Cu after pre-reduction up to  $-0.5 \text{ V}$  and stays reduced during electrolysis at higher bias. No evidence of residual Cu oxides on the electrode surface is detected by XPS when transferred to the analysis chamber under inert atmosphere, contrasting the above observations from ex situ soft XAS following brief air exposure, and validating the usefulness of the air-free transfer methodology.

A similar behavior was observed for Cu in CuNW-Sn<sub>LOW</sub>—it appears to be fully reduced to metallic Cu<sup>0</sup> after CP activation up to  $-0.5 \text{ V}$  and remains reduced after CO<sub>2</sub> electrolysis at  $-0.7$  and  $-0.9 \text{ V}$  (Figure 4 a,b). As observed in the soft-XAS measurements, the sample CuNW-Sn<sub>HIGH</sub> does not show any Cu-related signals in the AS state, indicating that the SnO<sub>2</sub>



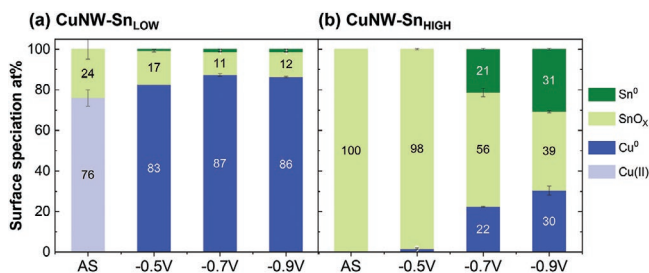


**Figure 5.** Surface metal speciation derived from XPS analysis, expressed as at. % of each species relative to total metal (Cu+Sn) for a) CuNW-Sn<sub>LOW</sub> and b) CuNW-Sn<sub>HIGH</sub>, following CO<sub>2</sub> electrolysis at the indicated potential and air-free transfer to the XPS analysis chamber.

ALD layer ( $\approx 20$  nm) covers all the CuNW surface (Figure 4a,b). After CP pre-reduction up to  $-0.5$  V an incipient Cu 2p signal appears at the position expected for metallic Cu<sup>0</sup> indicating that a SnO<sub>2</sub> ALD layer remains enriched at the catalyst surface after the CP pre-reduction step, as previously observed by soft XAS (Figure S13b, Supporting Information). After CO<sub>2</sub> electrolysis at  $-0.7$  V and  $-0.9$  V, typical Cu 2p and Cu LMM spectral features assigned to metallic Cu<sup>0</sup> are dominant, indicating a full reduction of Cu and its migration from core to surface during CO<sub>2</sub> electrolysis (Figure 4a,b).

The investigation of the progressive reduction of the SnO<sub>2</sub> layer by XPS (Figure 4c) indicates different Sn speciation in CO-selective (CuNW-Sn<sub>LOW</sub>) and formate-selective (CuNW-Sn<sub>HIGH</sub>) catalysts. In the AS state, both display a doublet with the main peak for the Sn 3d<sub>5/2</sub> component at BE 486.7 eV in agreement with the reported value for SnO<sub>2</sub>.<sup>[29,30]</sup> CuNW-Sn<sub>LOW</sub> exhibits a slight shift towards lower BE 486.5 eV after CP activation to  $-0.5$  V, indicating a partial reduction to SnO (i.e., Sn<sup>2+</sup>), as well as peak broadening which may indicate a mixed contribution of both Sn<sup>2+</sup> and Sn<sup>4+</sup> oxidation states. Due to this convolution, we denote this composition as SnO<sub>x</sub>. After CO<sub>2</sub> electrolysis at  $-0.7$  and  $-0.9$  V, a peak at 486.5 eV assigned to SnO<sub>x</sub> and a small shoulder at 485 eV assigned to metallic Sn<sup>0</sup> are observed (Figure 4c). The results indicate that following operation under all tested CO<sub>2</sub>ER conditions ( $-0.5$ ,  $-0.7$ , and  $-0.9$  V), CuNW-Sn<sub>LOW</sub> surface is composed of fully reduced metallic Cu<sup>0</sup> and Sn predominantly in an oxidized state (Figure 4c, Figure 5a). These results are in good agreement with the persistence of SnO<sub>x</sub> species observed for CuNW-Sn<sub>LOW</sub> by in situ Sn K-edge XANES (Figure S12b, Supporting Information) and provide experimental support for previous DFT studies which identify persistent oxidized Sn as a crucial selectivity director in Cu–Sn CO-selective catalysts.<sup>[22,28]</sup>

The surface composition and speciation results are summarized in Table 1 and Figure 5. The CuNW-Sn<sub>LOW</sub> catalyst surface displays an Sn fraction (relative to total Cu + Sn content) of 24 at. % in the AS condition, which decreases to 19 at. % after CP activation and at  $\approx 13$  at. % after electrolysis at  $-0.7$  and  $-0.9$  V. This Sn content is in line with surface composition reported in previous studies on low surface area CO-selective Cu–Sn catalysts<sup>[21,22,28]</sup> and Sn functionalized Cu foams.<sup>[23]</sup> The observed surface Sn content decrease after CO<sub>2</sub>ER is in agreement with the redistribution of Sn from the surface to the core reported by Schreier et al.<sup>[16]</sup> which is observed by STEM-EDX elemental mapping.

For the formate-selective catalyst, CuNW-Sn<sub>HIGH</sub>, the Sn 3d signal broadens but remains at the same position after CP pre-reduction, indicating that the SnO<sub>x</sub> ALD layer persists mostly unchanged, as observed by soft XAS (Figure S13, Supporting Information). Examination of electrodes after CO<sub>2</sub> electrolysis at  $-0.7$  and  $-0.9$  V, the Sn 3d spectra develop new peaks assigned to Sn<sup>2+</sup> (486.4 eV) and metallic Sn<sup>0</sup> (484.9 eV) (Figure 4c). Thus, after CO<sub>2</sub> electrolysis at  $-0.7$  and  $-0.9$  V the CuNW-Sn<sub>HIGH</sub> catalyst surface is composed of metallic Cu and a mixture of metallic Sn and SnO<sub>x</sub> (Figures 4c and 5b). The observation of persistent SnO<sub>x</sub> species following CO<sub>2</sub>ER in Cu–Sn formate-selective catalysts is in good agreement with Sn K-edge XANES experiments (Figure S12, Supporting Information) and a previous report on in situ Sn K-edge EXAFS.<sup>[18]</sup>

## 2.4. Microstructure Analysis by Electron Microscopy and Elemental Mapping

The structural transformation of CuNW-Sn<sub>HIGH</sub> during CO<sub>2</sub>ER was further investigated by TEM in the AS state and following CO<sub>2</sub>ER experiments at different applied biases. To minimize the impact of air exposure on post-electrolysis samples, every sample preparation, electrochemical testing, and TEM sample preparation were conducted inside a glovebox (as for quasi in situ XPS experiments). The post-electrolysis samples were then transferred under inert atmosphere into the TEM instrument. A brief exposure to air (<10 s) was unavoidable during sample loading.

The TEM characterization for CuNW-Sn<sub>HIGH</sub> is displayed in Figure 6. The AS sample shows CuO nanowires of approx. 100–200 nm diameter coated with an amorphous layer (Figure 6b). SAED analysis (Figure 6a) indicates that the wires are composed of CuO (C2/c) in agreement with GI-XRD (Figure S8, Supporting Information). Additionally, a broad diffuse ring ascribed to the SnO<sub>2</sub> amorphous layer is observed at d spacings between 2.7–3.3 Å where SnO<sub>2</sub> (P42/mnm) diffraction signals are expected. Detailed lattice spacing assignment information is provided in Table S4, Supporting Information. Energy-filtered transmission electron microscopy (EFTEM)<sup>[45,46]</sup> mapping (Figure 6c) provides further evidence of a conformal coating (15–25 nm) of SnO<sub>2</sub> along the CuNW structures, as expected from the ALD synthesis method and in agreement with the XPS results displaying exclusively SnO<sub>2</sub> at the catalyst surface (Figure 4a).

Following CO<sub>2</sub> electrolysis at  $-0.6$  V for 2 h, the SAED analysis (Figure 6d) indicates that the CuO nanowire core of the sample has been fully reduced to Cu<sup>0</sup> while the outer SnO<sub>2</sub> layer remains in a rather amorphous state as observed in TEM micrographs (Figure 6e) and indicated by the persistence of the diffuse broad diffraction ring ascribed to the SnO<sub>x</sub> amorphous layer. The EFTEM mapping further confirms the persistence of an Sn-enriched shell after electrolysis. HR-TEM analysis of the core-shell interface (Figure S14, Supporting Information) indicates that the outer shell is amorphous while at the interface small crystallites (<5 nm) are observed, with lattice spacings  $d = 2.8$ – $3.0$  Å ascribed to Cu<sub>6</sub>Sn<sub>5</sub> alloy or Sn<sup>0</sup> and  $d = 1.6$  and  $1.9$  Å ascribed to SnO. The results suggest that at  $-0.6$  V the SnO<sub>2</sub> layer persists as a SnO<sub>x</sub> amorphous layer with only

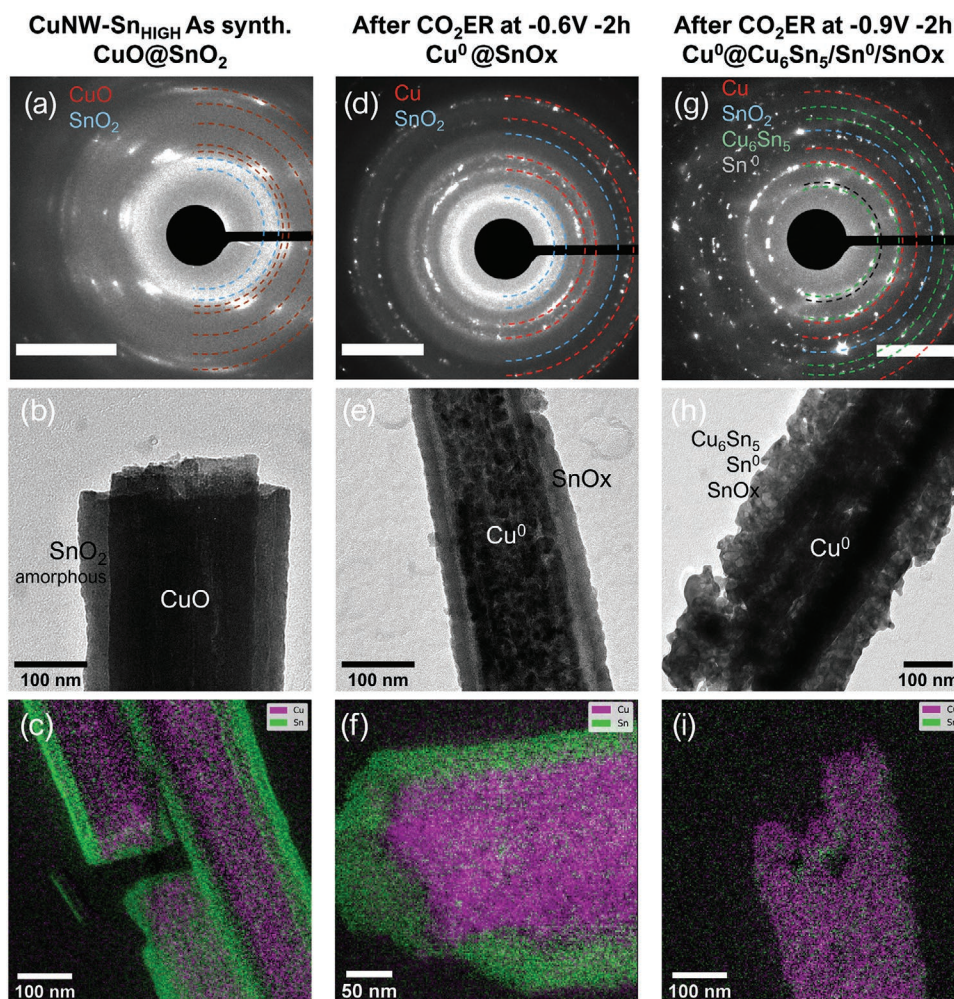


**Figure 6.** TEM characterization of a–c) CuNW-Sn<sub>HIGH</sub> AS, and after electrolysis at d–f) –0.6 and g–i) –0.9 V. Top images correspond to SAED analysis (scale bar 5 nm<sup>–1</sup>), middle images correspond to TEM micrographs and bottom images correspond to EFTEM mappings of Cu (L-edge: purple) and Sn (M-edge: green).

partial reduction to Cu<sub>6</sub>Sn<sub>5</sub> alloy, Sn<sup>0</sup>, and SnO at the interface with the Cu<sup>0</sup> nanowire core. These findings agree with previous observations of the persistence of an enriched SnO<sub>x</sub> layer at this potential by in situ Sn K-edge XAS (Figure S12, Supporting Information) and quasi in situ XPS (Figure 4).

As the reductive electrolysis bias is increased to –0.9 V, further structural changes were verified by TEM (Figure 6g–i). The TEM micrograph in Figure 6h shows that the outer layer appears crystalline in contrast with the same sample in AS condition and after CO<sub>2</sub>ER at –0.6 V. SAED analysis reveals that the diffuse rings assigned to the SnO<sub>x</sub> layer have disappeared after CO<sub>2</sub> electrolysis at –0.9 V (Figure 6g) while diffraction signals at  $d = 2.9, 2.8,$  and  $2.1 \text{ \AA}$  ascribed to Cu<sub>6</sub>Sn<sub>5</sub> or Sn<sup>0</sup> are observed, indicating the reduction of the SnO<sub>x</sub> layer. Nevertheless, a diffraction signal or ring at  $1.7 \text{ \AA}$  that could be ascribed to SnO<sub>2</sub> and SnO was also observed. The observation of lattice fringes in HR-TEM images of the shell (Figure S15, Supporting Information), as well as bright areas in dark-field images, confirm the presence of small crystallites (<5 nm) with lattice spacings concordant with Cu<sub>6</sub>Sn<sub>5</sub> or Sn<sup>0</sup> ( $d = 2.8\text{--}3.0 \text{ \AA}$ ) and SnO/SnO<sub>2</sub> ( $d = 1.6\text{--}1.9 \text{ \AA}$ ). Additionally, EFTEM mapping displays the

content of both Sn and Cu in the nanowire shell (Figure 6i) in contrast with the enriched SnO<sub>x</sub> shell observed after electrolysis at –0.6 V (Figure 6f). The results indicate that at this potential the electrolysis process leads to the reduction of the amorphous SnO<sub>x</sub> layer to Cu<sub>6</sub>Sn<sub>5</sub> and Sn<sup>0</sup>, mostly to Cu<sub>6</sub>Sn<sub>5</sub> as indicated by the predominance of the Cu<sub>6</sub>Sn<sub>5</sub> pattern over Sn<sup>0</sup> in GI-XRD pattern (Figure S8, Supporting Information) as well as the occurrence of both Cu and Sn in the catalyst shell. Indeed, the surface composition determined by XPS (Figure 5 and Table 1) demonstrates that CuNW-Sn<sub>HIGH</sub> catalyst surface is initially composed of SnO<sub>2</sub> exclusively ( $\approx 20 \text{ nm}$ ), which remains largely unaffected after CP pre-reduction (98 at. % Sn). However, after CO<sub>2</sub> electrolysis at –0.7 and –0.9 V the SnO<sub>x</sub> layer is reduced to Cu<sub>6</sub>Sn<sub>5</sub> alloy according to TEM-SAED (Figure 6g) and GI-XRD (Figure S8, Supporting Information) while Cu migrates from the CuNW core to the surface region, as confirmed by the EFTEM mapping (Figure 6i and Figure S16, Supporting Information), corresponding with a decrease in surface Sn content to 78 and 70 at. %, respectively (Figure 5). These results are in good agreement with the bulk composition of CuSn<sub>3</sub> reported for nanostructured formate-selective catalysts.<sup>[18]</sup>



Overall, the TEM investigation of structural changes in CuNW-Sn<sub>HIGH</sub> reveals the selective reduction of Cu and the persistence of the outer SnO<sub>x</sub> layer to yield a Cu<sup>0</sup>@SnO<sub>x</sub> core@shell structure at a low reductive bias (> −0.6 V), while high reductive bias < −0.7 V triggers a partial reduction of the outer SnO<sub>x</sub> layer predominantly to Cu<sub>6</sub>Sn<sub>5</sub> with the persistence of SnO<sub>x</sub> domains, in good agreement with the Sn speciation results investigated by quasi in situ XPS (Figure 4) and in situ Sn K-edge XANES (Figure S12, Supporting Information).

It is worth noting that the potentials where metallic Sn emerges at the surface (−0.7 V) correspond with the potentials at which formate selectivity increases to reach high selectivity of 80% at −0.9 V. In contrast, at less reductive potentials (>−0.6 V) where a Cu<sup>0</sup>@SnO<sub>x</sub> core@shell structure is observed (see XPS Figure 4, XRD Figure S8, Supporting Information, and TEM Figure 6d–f), H<sub>2</sub> is the dominant product (Figure 2d). While the persistence of surface SnO<sub>x</sub> moieties has been demonstrated as beneficial for formate selectivity in pure Sn catalysts,<sup>[29–31,47]</sup> our results indicate that only when reduced metallic Sn<sup>0</sup> is formed at the catalyst surface, high formate selectivity is observed, indicating that metallic Sn<sup>0</sup> sites play a crucial role in formate production pathway.

Another interesting effect in CuNW-Sn catalysts is the decrease in surface Sn content observed by XPS after CO<sub>2</sub>ER testing for both samples, CuNW-Sn<sub>LOW</sub> and CuNW-Sn<sub>HIGH</sub> (Figure 5 and Table 1). This Sn decrease is presumably due to a combined effect of Cu migration from the CuNW core to the surface during electrolysis (as previously reported by Schreier et al.<sup>[16]</sup> and further confirmed in this study by EFTEM mapping and XPS) and a partial Sn loss, as evidenced by the decrease of bulk Sn content observed by SEM-EDX and further confirmed by ICP-OES analysis of electrolyte samples (Table S1, Supporting Information). In view of this dynamic surface composition, the CO<sub>2</sub>ER activity and surface composition in CuNW-Sn<sub>LOW</sub> and CuNW-Sn<sub>HIGH</sub> were investigated for extended electrolysis duration (Figure S17, Supporting Information). The product selectivity and surface composition exhibit negligible changes over this extended time, indicating that the redistribution of Cu–Sn at the surface occurs early during CO<sub>2</sub> electrolysis and stabilizes over time. Taken together, our observations (electrochemical and spectroscopic) all indicate that the major transformations happen early during an “activation” period and then stabilize into a structure that persists afterwards, maintaining the structure and activity which dictates the catalytic selectivity.

Overall, the “quasi in situ XPS” experiments demonstrate that in all CuNW samples the Cu is readily reduced to Cu<sup>0</sup> during CP pre-reduction at mild reductive bias and remains reduced after CO<sub>2</sub> electrolysis at −0.7 and −0.9 V. The observation of surface Cu present exclusively as metallic Cu (Figure 5) indicates that at least within the XPS detection limit no oxidation of surface Cu occurs due to the removal of reductive bias removal during sample handling under inert atmosphere. The results correlate with bulk Cu reduction observed in situ by hard X-ray spectroscopy (Figure 3) and demonstrate the efficacy of the quasi in situ approach to protect surface Cu from oxidation in air. The oxidation state in pure Cu catalysts during CO<sub>2</sub>ER has been widely investigated and remains a topic of debate.<sup>[48]</sup> Some studies have found evidence of persistence of

surface or subsurface oxide<sup>[38,39,49,50]</sup> while our observation of full reduction to Cu<sup>0</sup> under CO<sub>2</sub>ER conditions is in agreement with recent investigations performed by in situ XAS<sup>[35,51,52]</sup> and quasi in situ XPS<sup>[53]</sup> for pure Cu catalysts. In the context of a bimetallic Cu–Sn structure, it is interesting to note that the functionalization of the Cu(OH)<sub>2</sub> nanowires with SnO<sub>2</sub> does not affect their full reduction to Cu<sup>0</sup>.

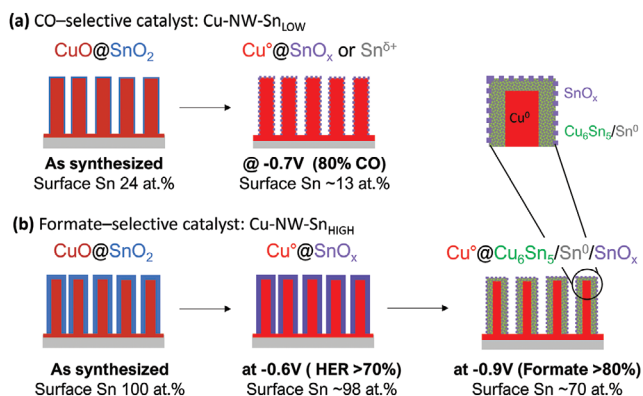
Regarding the Sn speciation investigated by “quasi in situ XPS”, SnO<sub>x</sub> surface moieties have been observed after CO<sub>2</sub>ER tests at potentials as reductive as −0.9 V. While we cannot exclude that the observed SnO<sub>x</sub> species are at least partially created upon bias removal even under complete O<sub>2</sub>-free handling, the in situ Sn K-edge XANES study further confirmed that SnO<sub>x</sub> moieties are indeed present during CO<sub>2</sub>ER at reductive bias as high as −0.9 V (Figure S12, Supporting Information). As stated above for Cu, the good correlation of observations on Sn speciation by in situ XAS and quasi in situ XPS demonstrate the persistence of SnO<sub>x</sub> species during CO<sub>2</sub>ER and validate the observations gathered by the quasi in situ approach and the efficacy of handling the post-electrolysis samples under inert atmosphere to minimize the impact of air oxidation in surface composition analysis. It is worth noting that the surface speciation assessed by XPS reveals a larger contribution of SnO<sub>x</sub> (Figures 4 and 5) in contrast with the larger Sn<sup>0</sup> contribution observed Sn K-edge XANES spectra (Figure S12, Supporting Information). This variation likely arises due to the different probing depths of the techniques. XPS is more surface sensitive, providing information on the outermost shell (< 3 nm) of the material in direct contact with electrolyte which is more likely to persist oxidized. In contrast, Sn-Kedge XANES probes the entire cross-section of the material and provides more bulk-sensitive information dominated by the reduced Cu<sub>6</sub>Sn<sub>5</sub> and Sn<sup>0</sup> grains formed during electrolysis at high bias as observed by the TEM study (Figure 6 and Figure S15, Supporting Information).

## 2.5. Effects of Air Exposure

To investigate the impact of air exposure in the surface composition of Cu–Sn bimetallic catalysts, some “post-electrolysis” samples were remeasured by XPS after intentional exposure to air for a duration of 20 min (labeled “air” in Figure 4). Minor changes are observed on the Cu 2p and Cu LMM spectra for bare CuNW and CuNW-Sn<sub>HIGH</sub> indicating the presence of small amounts of Cu<sub>2</sub>O. However, the CuNW-Sn<sub>LOW</sub> sample displays growth of Cu<sup>2+</sup> shake-up structure in the Cu 2p spectrum, and the Cu LMM Auger spectrum was found to be composed of a mix of Cu<sup>0</sup>, Cu<sub>2</sub>O, and Cu(OH)<sub>2</sub> (Figure 4a,b). These results are in good agreement with the observation of persistent Cu<sup>2+</sup> signal in ex situ soft XAS Cu L-edge spectra (Figure S13a, Supporting Information). The quasi in situ XPS experiments demonstrate, however, that the oxidized Cu<sup>+</sup>/Cu<sup>2+</sup> signals observed in the ex situ XAS study are generated during the brief period of exposure to air, which suggests that the modification of CuNW structures with low Sn content may facilitate the oxidation of Cu<sup>0</sup> in air.

Furthermore, and most significantly, the metallic Sn<sup>0</sup> formed after CO<sub>2</sub> electrolysis at −0.7 and −0.9 V is quickly re-oxidized





**Scheme 1.** Structural transformation during CO<sub>2</sub>ER at different applied bias for a) CO-selective catalyst: Cu-NW-Sn<sub>LOW</sub> and b) Formate-selective catalyst: Cu-NW-Sn<sub>HIGH</sub>.

in air, displaying spectra mostly composed by SnO<sub>x</sub> (Figure 4c bottom). Further details on the effect of air exposure are discussed in Section S7 and Figure S18, Supporting Information.

Interestingly, air exposure can also influence the Cu/Sn surface quantification. As an example, after CO<sub>2</sub>ER at -0.9 V the total Sn surface content determined by XPS on the CuNW-Sn<sub>HIGH</sub> sample increases from 70 to 77 at. % after air exposure (Table 1), while for CuNW-Sn<sub>LOW</sub> under similar conditions there is no significant change in Sn content. These observations confirm that ex situ characterization of catalysts conducted “post-mortem” after electrochemical testing and with air exposure can be susceptible to significant changes in surface speciation and quantification due to fast oxidation of metal surfaces in air, and migration of oxophilic metals such as Sn towards the surface upon air exposure.

The quasi in situ XPS results demonstrate that conducting electrochemical testing in an O<sub>2</sub>-free environment and transferring the samples under an inert atmosphere to the XPS analysis chamber can successfully prevent surface re-oxidation and allows one to analyze the catalyst surface as close as possible to in situ conditions in the absence of more sophisticated and challenging approaches such as near ambient pressure (NAP) XPS.<sup>[54–56]</sup>

## 2.6. Structure-Activity Correlations Using DFT

The detailed investigation of the structural transformation in oxide-derived CuNW-Sn catalysts during CO<sub>2</sub>ER testing presented in previous sections identified the structures of the CO-selective and formate-selective CuNW-Sn catalysts in their active and most selective form. The CO-selective catalyst, CuNW-Sn<sub>LOW</sub> is transformed from an original CuO@SnO<sub>2</sub> core@shell to a Cu<sup>0</sup>-SnO<sub>x</sub> structure during CO<sub>2</sub>ER as depicted in **Scheme 1a**. The optimal CO selectivity is observed at a medium bias of -0.7 V with an Sn surface content of ~13 at. %. The formate-selective catalyst CuNW-Sn<sub>HIGH</sub> is also transformed from an original CuO@SnO<sub>2</sub> core@shell to a Cu<sup>0</sup>@SnO<sub>x</sub> structure at mild reductive bias ( $E > -0.6$  V) where H<sub>2</sub> is observed as a major product, while more reductive potentials ( $E < -0.7$  V) trigger the partial reduction of the outer SnO<sub>x</sub> layer to Cu<sub>6</sub>Sn<sub>5</sub>

and Sn<sup>0</sup> with evidence of persistent SnO<sub>x</sub> domains to yield a Cu<sup>0</sup>@Cu<sub>6</sub>Sn<sub>5</sub>/Sn<sup>0</sup>/SnO<sub>x</sub> structure, which produces formate with high selectivity. These observations are summarized in Scheme 1b. Considering that the metallic Cu core in the wires is buried under the Cu<sub>6</sub>Sn<sub>5</sub>/Sn<sup>0</sup>/SnO<sub>x</sub> layer, its participation in the catalysis towards formate production is unlikely. The correlation of the outer layer composition and speciation suggests that the metallic Sn sites in Cu<sub>6</sub>Sn<sub>5</sub> and Sn<sup>0</sup> phases that emerge at high reductive bias ( $E < -0.7$  V) are essential to the formate production pathway and therefore these phases were investigated as models in the DFT mechanistic study detailed below.

To understand the influence of Cu-Sn surface structure on CO<sub>2</sub>ER selectivity, we employed DFT on selected models with the PBE functional (Section S8, Supporting Information, **Figure 7a**).<sup>[58]</sup> Different systems were considered depending on the experimentally-observed correlations between surface speciation and product selectivity (Scheme 1). To model the CO-evolving catalysts characterized by overall Sn content around 13 at. %, we built Cu(111) (3 × 3) and Cu(100) (3 × 3) supercells and substituted three surface Cu atoms with Sn (Figure 7a), thus equating to an Sn content of 11 at. %. The Bader charge analysis of Cu(111) (3 × 3) 11 at. % Sn model indicates a positive polarization of the Sn sites of around +0.6 |e| (Table S5, Supporting Information), in agreement with the presence of SnO<sub>x</sub> or Sn<sup>δ+</sup> observed for CuNW-Sn<sub>LOW</sub> by in situ XAS and quasi in situ XPS. Cu(111) (3 × 3) and Cu(100) (3 × 3) related models with 1 surface Sn substituent (4 Sn at. %) were investigated for comparison. As for the HCOO<sup>-</sup>-selective catalysts, we chose two models, Sn(100) (1 × 1) and Cu<sub>6</sub>Sn<sub>5</sub> (102) (1 × 1),<sup>[59,60]</sup> since formate selectivity in CuNW-Sn<sub>HIGH</sub> increased upon formation of Sn<sup>0</sup> in metallic Sn and Cu<sub>6</sub>Sn<sub>5</sub> phases (Figure 4c and Table 1). The chosen Cu, Sn, and Cu<sub>6</sub>Sn<sub>5</sub> facets present the lowest surface energies (Table S6, Supporting Information), and are thus expected to be the most abundant orientations on nanoparticles according to the Wulff theorem under equilibrium.<sup>[61]</sup> To further assess the reactivity of residual SnO<sub>x</sub> species and undercoordinated Sn sites, we built two epitaxial supercells, SnO<sub>2</sub>(110) (4 × 3)/Sn(100) (2 × 3) and SnO(001) (3 × 5)/Sn(100) (2 × 3), see Figure S19, Supporting Information. SnO<sub>2</sub>(110) and SnO(001) were chosen since they are the most stable crystalline facets for these oxides.<sup>[62]</sup> After depletion of surface oxygens to achieve an overall Sn content of 84 and 73 at. % for SnO<sub>2</sub>/Sn and SnO/Sn respectively, we optimized both systems through ab initio molecular dynamics to allow surface reconstruction (Section S8, Supporting Information).

On transition metals, the pathway for CO<sub>2</sub>ER to CO and HCOO<sup>-</sup> is assumed to bifurcate at an early stage (Figure 7b).<sup>[57]</sup> Carbon monoxide is formed upon adsorption of CO<sub>2</sub> in a  $\eta^2_{C,O}$  or  $\eta^1_C$  configuration via an ET, followed by a proton transfer (PT) which leads to a \*COOH intermediate (Figure 7b, red path). The OH group is then protonated via a proton-coupled electron transfer (PCET) and H<sub>2</sub>O desorbs, leaving a \*CO species on the surface. Finally, \*CO desorbs through a chemical step. Alternatively, formate production occurs via adsorption of CO<sub>2</sub> through its terminal oxygens ( $\eta^2_{O,O}$ ) favored by an ET, followed by a PT to the carbon atom and desorption of \*HCOO as HCOO<sup>-</sup> (Figure 7b, green path). CO<sub>2</sub> adsorption and protonation can as well occur as PCET steps, as considered by previous theoretical studies on copper-tin alloys.<sup>[28,63]</sup> In this study, we will

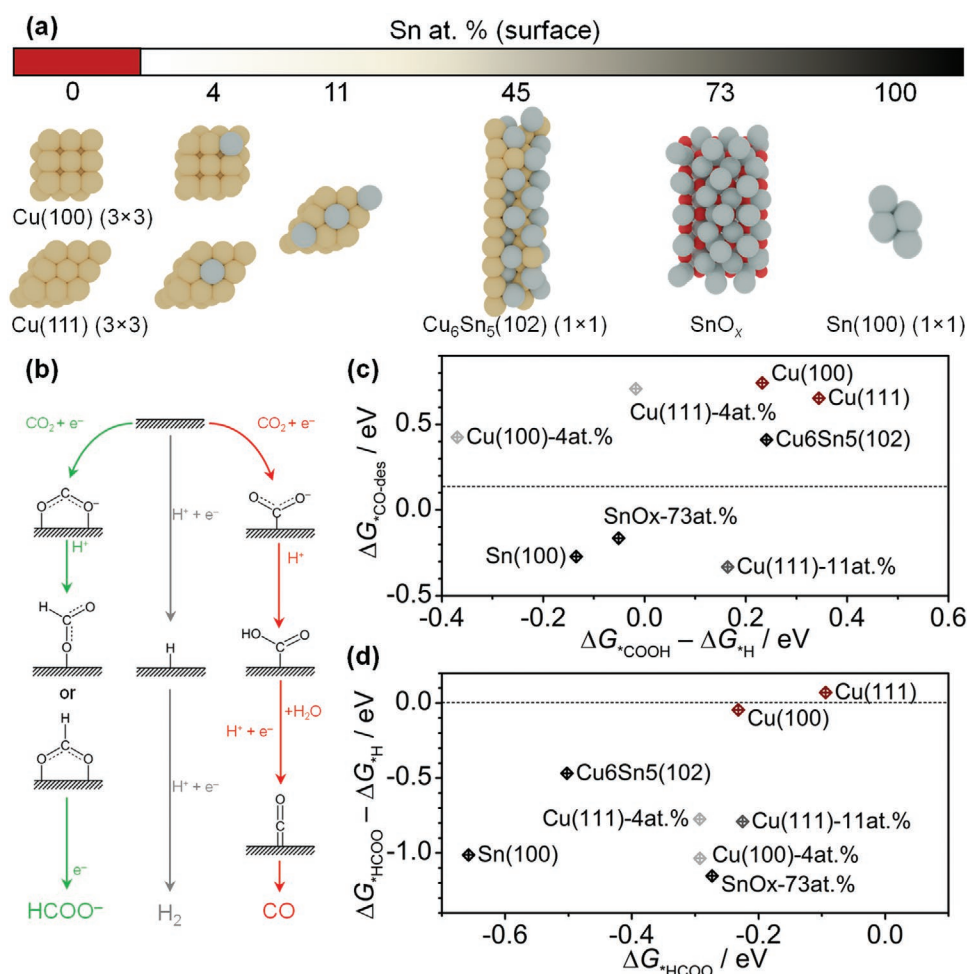


**Figure 7.** a) Models for DFT simulations at different Sn atomic ratio: Cu(100) (3 × 3) and Cu(111) (3 × 3) (0 Sn at. %); three Cu–Sn solid solutions with 1 to 3 Sn surface substituents in the Cu supercell (overall Sn content of 4–11 at. %); Cu<sub>6</sub>Sn<sub>5</sub>(102) (1 × 1) (45 at. % Sn); SnO<sub>x</sub> model (73 at. % Sn, see Figure S19, Supporting Information) and Sn(100) (1 × 1) (100 Sn.%). Light brown and grey balls represent Cu and Sn, respectively. b) Pathways for CO<sub>2</sub>ER to HCOO<sup>-</sup> and CO and HER, respectively defined in green, grey, and red, as defined from the state-of-the-art.<sup>[57]</sup> c)  $\Delta G_{\text{CO-des}}^*$  (y-axis) and  $\Delta G_{\text{COOH}}^* - \Delta G_{\text{H}}^*$  (x-axis) as descriptors for CO selectivity: Cu(111)-11at. %Sn and SnO<sub>x</sub>-73at. % bind COOH and H isoenergetically, yet allowing an exergonic desorption of CO ( $\Delta G_{\text{CO-des}}^* \leq 0$ ). d)  $\Delta G_{\text{HCOO}}^* - \Delta G_{\text{H}}^*$  (y-axis) and  $\Delta G_{\text{HCOO}}^*$  (x-axis) as effective descriptors for CO selectivity: increasing Sn content leads to stronger <sup>\*</sup>HCOO binding and weaker H binding, thus enabling CO<sub>2</sub>ER to HCOO<sup>-</sup> in detriment of HER.

apply the latter reaction scheme for consistency. The HER competes with CO<sub>2</sub>ER under cathodic bias. State-of-the-art modeling usually assumes HER to proceed via reduction of an adsorbed proton and its successive coupling with a second proton either adsorbed or from solution (Figure 7b, grey path).<sup>[57]</sup>

Bagger et al. proposed a thermoneutral CO binding energy as a key property of catalysts evolving CO, while they attributed a high performance toward formic acid to a highly endergonic <sup>\*</sup>H adsorption.<sup>[64]</sup> Pure copper displays low CO selectivity (Figure 2a), as CO desorption is endergonic by 0.5 eV (Figure 7c, Figure S20, Supporting Information),<sup>[64]</sup> while faradaic efficiencies toward hydrogen and formate on Cu are both ≈40% at −0.7 V versus RHE (Figure 2a) since H and HCOO<sup>-</sup> binding energies are nearly equivalent (Figure 7d, Figure S21, Supporting Information).

In contrast, the Cu(111)-11at. Sn% model presents the weakest CO binding energy among the considered systems (Figure 7c), yet shows nearly equivalent energetics for <sup>\*</sup>COOH

and <sup>\*</sup>H adsorptions. Thus, the reduction pathway toward CO is open at −0.7 V versus RHE (Figure S20, Supporting Information), in excellent agreement with experimental results for the CuNW-Sn<sub>LOW</sub> catalysts with 13 at. % Sn content (Figure 2c). In the Sn enriched models, pure Sn and Cu<sub>6</sub>Sn<sub>5</sub> have the strongest HCOO<sup>-</sup> binding energies and HCOO<sup>-</sup> adsorbs more favorably than H by at least 0.5 eV (Figure 7d). Hence, the pathway toward formate is increasingly more favorable than HER for higher content of Sn, leading to the >80% FE toward formate at −0.9 V versus RHE for the CuNW-Sn<sub>HIGH</sub> sample (Figure 2d, Figure S21, Supporting Information). In general, the SnO<sub>x</sub> model exhibits weaker <sup>\*</sup>HCOO, <sup>\*</sup>COOH, and <sup>\*</sup>H binding energies than Sn(100) (Figure 7d, Table S7, Supporting Information), thus motivating the poor CO<sub>2</sub>R reduction performance of the Cu<sup>0</sup>@SnO<sub>x</sub> system at −0.6 V (Scheme 1b).

The modulation of CO<sub>2</sub>ER selectivity observed with increasing Sn content, making Cu–Sn first selective toward CO and then to HCOO<sup>-</sup>, is caused by changes in the electronic

state of Sn. As proposed by Vasileff et al.,<sup>[28]</sup> for low Sn content, the copper matrix withdraws electronic density from Sn sites, as predicted by Bader charge analysis (Table S5, Supporting Information). The Sn<sup>δ+</sup> sites destabilize CO adsorption on Cu sites, thus enabling the subsequent release of CO which is hindered on the pure copper system. In the Sn enriched models (Sn ≥ 45 at. %)—Cu<sub>6</sub>Sn<sub>5</sub> and pure Sn—this localized effect is absent, since Sn sites are mainly metallic for both systems (according to Bader charge analysis, Table S5, Supporting Information). These Sn<sup>0</sup> sites are responsible for a weaker H binding and stronger HCOO<sup>−</sup> adsorption, thus making CO<sub>2</sub>ER formate more favorable than HER.<sup>[64]</sup> Furthermore, at high Sn content, the relatively close proximity of Sn sites to one another leads to ensemble effects that strengthen adsorption of CO<sub>2</sub> through its terminal oxygens ( $\eta^2_{\text{O}_2}$ ), which opens the formate pathway.

### 3. Conclusions

Cu(OH)<sub>2</sub> nanowire array electrodes modified by SnO<sub>2</sub> ALD overlayers were optimized to reach high selectivity towards either CO or formate depending on the number of ALD cycles (15 or 182 cycles, respectively) with negligible differences in electrode morphology. These Cu–Sn mixed oxide composites were studied via a comprehensive investigation of metal oxidation states and chemical environments following progressive reduction of the materials during CO<sub>2</sub>ER by bulk sensitive hard XAS, and surface-sensitive soft X-ray absorption and XPS, in order to reach a better understanding of Cu–Sn synergetic effects.

Our results indicate that Cu–Sn-based CO-selective catalysts display optimal selectivity at a medium bias of −0.7 V, where their surface is composed of metallic Cu and SnO<sub>x</sub> with an Sn surface content of ≈13 at. %. On the other hand, formate-selective catalysts display optimal selectivity at a higher bias of −0.9 V, under these conditions their surface is composed of metallic Cu and a mixture of metallic Sn and SnO<sub>x</sub>, with an Sn surface content of ≈70 at. %. The correlation of Sn surface speciation with CO<sub>2</sub>ER selectivity in the formate-selective catalyst indicates that metallic Sn sites enable high formate selectivity. DFT simulations indicate two regimes on Cu–Sn catalysts. At low Sn content, localized electronic effects lead to the formation of Sn<sup>δ+</sup>, which weaken CO adsorption on Cu and thus enable CO formation. For Sn content ≥ 45 the overall system shows similar reactivity as pure Sn, hindering H adsorption while promoting formate production. Further improvement of Cu–Sn catalysts performance by increasing the catalytic current density may be achieved by targeting the above-mentioned surface compositions through functionalization of high surface area Cu nanostructures with Sn overlayers integrated into gas diffusion electrode configurations.<sup>[65]</sup> Such approaches can potentially enable selective and energy-efficient CO or formate production at practical conversion rates using earth-abundant catalyst materials.

Overall, the complementary information gathered by bulk and surface sensitive characterization techniques has allowed us to unravel the complex and dynamic nature of structural and compositional changes observed in Cu–Sn bimetallic electrocatalysts under CO<sub>2</sub>ER turnover. Our findings highlight the importance of conducting thorough structural

characterization by in situ or quasi in situ approaches with consideration to bulk versus surface sensitivity, and, when possible, avoiding ambient conditions (such as air exposure) which can drastically affect observed composition and speciation. In situ studies by hard XAS can reveal structural information under true operating conditions, but this typically requires a synchrotron and furthermore gives predominantly bulk-sensitive information. Methods which are mostly surface-sensitive (such as soft XAS and XPS) are more challenging to accomplish in situ, so a good compromise is to conduct electrocatalyst testing and then transfer the samples to the analysis chamber under inert atmosphere, in order to study the electrode material as close as possible to relevant catalytic conditions.

### 4. Experimental Section

Complete details regarding materials and methods are provided in the Supporting Information file.

### Supporting Information

Supporting Information is available from the Wiley Online Library or from the author.

### Acknowledgements

This work was supported by the Helmholtz Association's Initiative and Networking Fund (Helmholtz Young Investigator Group VH-NG-1225) and the Helmholtz Climate Initiative (Net-Zero-2050). The research utilized instrumentation within the Helmholtz Energy Materials Foundry (HEMF), the HySPRINT Helmholtz Innovation Lab, the HZB X-ray core lab, the HZB corelab Correlative Microscopy and Spectroscopy, and the HZB Institute for Solar Fuels. The authors thank HZB for the allocation of beamtime at the BESSY II synchrotron where X-ray absorption measurements were conducted at beamlines KMC-2, UE56-2\_PGM-2 and BAMline. J.T.A., F.D., and N.L. acknowledge the financial support from the European Union (project FlowPhotoChem 862453-FLOWPHOTO-CHEM), from the Spanish Ministry of Science and Innovation ("Severo Ochoa Center", MCIN/AEI/10.13039/501100011033 CEX2019-000925-S), as well as the Barcelona Supercomputing Center (BSC-RES) for providing generous computational resources. The authors thank the following colleagues for experimental and technical support: Lifei Xi, Álvaro Díaz Duque, Christian Höhn, Karsten Harbauer, Ursula Michalczyk, Kirill Yusenko, René Gunder, and Michael Tovar.

Open access funding enabled and organized by Projekt DEAL.

### Conflict of Interest

The authors declare no conflict of interest.

### Data Availability Statement

The data that support the findings of this study are available from the corresponding author upon reasonable request. The density functional theory data sets generated during the current study are available in the ioChem-BD database<sup>[66]</sup> at DOI: <https://doi.org/10.19061/iochem-bd-1-211>.



## Keywords

CO<sub>2</sub> conversion, electrocatalysis, non-noble catalysts, X-ray spectroscopy

Received: October 25, 2021

Revised: December 6, 2021

Published online:

- [1] K. P. Kuhl, E. R. Cave, D. N. Abram, T. F. Jaramillo, *Energy Environ. Sci.* **2012**, 5, 7050.
- [2] J. B. Greenblatt, D. J. Miller, J. W. Ager, F. A. Houle, I. D. Sharp, *Joule* **2018**, 2, 381.
- [3] S. Sen, D. Liu, G. T. R. Palmore, *ACS Catal.* **2014**, 9, 3091.
- [4] A. Dutta, M. Rahaman, M. Mohos, A. Zanetti, P. Broekmann, *ACS Catal.* **2017**, 7, 5431.
- [5] K. D. Yang, W. R. Ko, J. H. Lee, S. J. Kim, H. Lee, M. H. Lee, K. T. Nam, *Angew. Chem., Int. Ed.* **2017**, 56, 796.
- [6] K. Klingan, T. Kottakatt, Z. P. Jovanov, S. Jiang, C. Pasquini, F. Scholten, P. Kubella, A. Bergmann, B. Roldan Cuenya, C. Roth, H. Dau, *ChemSusChem* **2018**, 11, 3449.
- [7] F. S. Roberts, K. P. Kuhl, A. Nilsson, *Angew. Chem., Int. Ed.* **2015**, 54, 5179.
- [8] C. W. Li, J. Ciston, M. W. Kanan, *Nature* **2014**, 508, 504.
- [9] M. Ma, K. Djanashvili, W. A. Smith, *Phys. Chem. Chem. Phys.* **2015**, 17, 20861.
- [10] Y. Lum, B. Yue, P. Lobaccaro, A. T. Bell, J. W. Ager, *J. Phys. Chem. C* **2017**, 121, 14191.
- [11] H. Mistry, A. S. Varela, C. S. Bonifacio, I. Zegkinoglou, I. Sinev, Y. W. Choi, K. Kisslinger, E. A. Stach, J. C. Yang, P. Strasser, B. R. Cuenya, *Nat. Commun.* **2016**, 7, 12123.
- [12] D. Ren, Y. Deng, A. D. Handoko, C. S. Chen, S. Malkhandi, B. S. Yeo, *ACS Catal.* **2015**, 5, 2814.
- [13] S. Nitopi, E. Bertheussen, S. B. Scott, X. Liu, A. K. Engstfeld, S. Horch, B. Seger, I. E. L. Stephens, K. Chan, C. Hahn, J. K. Nørskov, T. F. Jaramillo, I. Chorkendorff, *Chem. Rev.* **2019**, 119, 7610.
- [14] A. Vasileff, C. Xu, Y. Jiao, Y. Zheng, S. Z. Qiao, *Chem* **2018**, 4, 1809.
- [15] M. K. Birhanu, M.-C. Tsai, A. W. Kahsay, C.-T. Chen, T. S. Zeleke, K. B. Ibrahim, C.-J. Huang, W.-N. Su, B.-J. Hwang, *Adv. Mater. Interfaces* **2018**, 5, 1800919.
- [16] M. Schreier, F. Héroguel, L. Steier, S. Ahmad, J. S. Luterbacher, M. T. Mayer, J. Luo, M. Grätzel, *Nat. Energy* **2017**, 2, 17087.
- [17] S. Sarfraz, A. T. Garcia-Esparza, A. Jedidi, L. Cavallo, K. Takanabe, *ACS Catal.* **2016**, 6, 2842.
- [18] K. Ye, Z. Zhou, J. Shao, L. Lin, D. Gao, N. Ta, R. Si, G. Wang, X. Bao, *Angew. Chem., Int. Ed.* **2020**, 59, 4814.
- [19] X. Hou, Y. Cai, D. Zhang, L. Li, X. Zhang, Z. Zhu, L. Peng, Y. Liu, J. Qiao, *J. Mater. Chem. A* **2019**, 7, 3197.
- [20] A. Vasileff, C. Xu, L. Ge, Y. Zheng, S. Z. Qiao, *Chem. Commun.* **2018**, 54, 13965.
- [21] M. Morimoto, Y. Takatsui, R. Yamasaki, H. Hashimoto, I. Nakata, T. Sakakura, T. Haruyama, *Electrocatalysis* **2018**, 9, 323.
- [22] Q. Li, J. Fu, W. Zhu, Z. Chen, B. Shen, L. Wu, Z. Xi, T. Wang, G. Lu, J. J. Zhu, S. Sun, *J. Am. Chem. Soc.* **2017**, 139, 4290.
- [23] J. Zeng, K. Bejtka, W. Ju, M. Castellino, A. Chiodoni, A. Sacco, M. A. Farkhondeh, S. Hernández, D. Rentsch, C. Battaglia, C. F. Pirri, *Appl. Catal., B* **2018**, 236, 475.
- [24] W. Ju, J. Zeng, K. Bejtka, H. Ma, D. Rentsch, M. Castellino, A. Sacco, C. F. Pirri, C. Battaglia, *ACS Appl. Energy Mater.* **2019**, 2, 867.
- [25] S. Stojković, G. A. El-Nagar, F. Firsche, L. C. Pardo Pérez, L. Choubrac, M. Najdoski, M. T. Mayer, *ACS Appl. Mater. Interfaces* **2021**, 13, 38161.
- [26] Y. Zhao, C. Wang, G. G. Wallace, *J. Mater. Chem. A* **2016**, 4, 10710.
- [27] C. Chen, Y. Pang, F. Zhang, J. Zhong, B. Zhang, Z. Cheng, *J. Mater. Chem. A* **2018**, 6, 19621.
- [28] A. Vasileff, X. Zhi, C. Xu, L. Ge, Y. Jiao, Y. Zheng, S. Z. Qiao, *ACS Catal.* **2019**, 9, 9411.
- [29] Y. Chen, M. W. Kanan, *J. Am. Chem. Soc.* **2012**, 134, 1986.
- [30] S. Zhang, P. Kang, T. J. Meyer, *J. Am. Chem. Soc.* **2014**, 136, 1734.
- [31] D. H. Won, C. H. Choi, J. Chung, M. W. Chung, E. H. Kim, S. I. Woo, *ChemSusChem* **2015**, 8, 3092.
- [32] Helmholtz-Zentrum Berlin für Materialien und Energie, *J. large-scale Res. Facil.* **2016**, 2, A49.
- [33] B. L. Henke, E. M. Gullikson, J. C. Davis, *At. Data Nucl. Data Tables* **1993**, 54, 181.
- [34] G. S. Henderson, F. M. F. de Groot, B. J. A. Moulton, *Rev. Mineral. Geochem.* **2014**, 78, 75.
- [35] S. H. Lee, J. C. Lin, M. Farmand, A. T. Landers, J. T. Feaster, J. E. Avilés Acosta, J. W. Beeman, Y. Ye, J. Yano, A. Mehta, R. C. Davis, T. F. Jaramillo, C. Hahn, W. S. Drisdell, *J. Am. Chem. Soc.* **2021**, 143, 588.
- [36] M. Farmand, A. T. Landers, J. C. Lin, J. T. Feaster, J. W. Beeman, Y. Ye, E. L. Clark, D. Higgins, J. Yano, R. C. Davis, A. Mehta, T. F. Jaramillo, C. Hahn, W. S. Drisdell, *Phys. Chem. Chem. Phys.* **2019**, 21, 5402.
- [37] H. Riesemeier, K. Ecker, W. Görner, B. R. Müller, M. Radtke, M. Krumrey, *X-Ray Spectrom.* **2005**, 34, 160.
- [38] F. Cavalca, R. Ferragut, S. Aghion, A. Eilert, O. Diaz-Morales, C. Liu, A. L. Koh, T. W. Hansen, L. G. M. Pettersson, A. Nilsson, *J. Phys. Chem. C* **2017**, 121, 25003.
- [39] A. Eilert, F. Cavalca, F. S. Roberts, J. Osterwalder, C. Liu, M. Favaro, E. J. Crumlin, H. Ogasawara, D. Friebe, L. G. M. Pettersson, A. Nilsson, *J. Phys. Chem. Lett.* **2017**, 8, 285.
- [40] Helmholtz-Zentrum Berlin für Materialien und Energie, *J. large-scale Res. Facil.* **2016**, 2, A80.
- [41] M. Abbate, J. B. Goedkoop, F. M. F. de Groot, M. Grioni, J. C. Fuggle, S. Hofmann, H. Petersen, M. Sacchi, *Surf. Interface Anal.* **1992**, 18, 65.
- [42] R. Qiao, I. T. Lucas, A. Karim, J. Syzdek, X. Liu, W. Chen, K. Persson, R. Kostecki, W. Yang, *Adv. Mater. Interfaces* **2014**, 1, 1300115.
- [43] J. Timoshenko, B. R. Cuenya, *Chem. Rev.* **2021**, 121, 882.
- [44] M. C. Biesinger, *Surf. Interface Anal.* **2017**, 49, 1325.
- [45] T. Heil, B. Gralla, M. Epping, H. Kohl, *Ultramicroscopy* **2012**, 118, 11.
- [46] B. Schaffer, G. Kothleitner, W. Grogger, *Ultramicroscopy* **2006**, 106, 1129.
- [47] M. F. Baruch, J. E. Pander, J. L. White, A. B. Bocarsly, *ACS Catal.* **2015**, 5, 3148.
- [48] Z.-Z. Wu, F.-Y. Gao, M.-R. Gao, *Energy Environ. Sci.* **2021**, 14, 1121.
- [49] M. Favaro, H. Xiao, T. Cheng, W. A. Goddard, J. Yano, E. J. Crumlin, *Proc. Natl. Acad. Sci. U. S. A.* **2017**, 114, 6706.
- [50] Y. Zhao, X. Chang, A. S. Malkani, X. Yang, L. Thompson, F. Jiao, B. Xu, *J. Am. Chem. Soc.* **2020**, 142, 9735.
- [51] N. J. Firet, T. Burdyny, N. T. Nesbitt, S. Chandrashekar, A. Longo, W. A. Smith, *Catal. Sci. Technol.* **2020**, 10, 5870.
- [52] J. J. Velasco-Velez, J. J. Velasco-Velez, R. V. Mom, L. E. Sandoval-Diaz, L. J. Felling, C. H. Chuang, D. Gao, D. Gao, T. E. Jones, Q. Zhu, Q. Zhu, R. Arrigo, B. Roldan Cuenya, A. Knop-Gericke, A. Knop-Gericke, T. Lunkenbein, R. Schlögl, R. Schlögl, *ACS Energy Lett.* **2020**, 5, 2106.
- [53] R. M. Arán-Ais, F. Scholten, S. Kunze, R. Rizo, B. R. Cuenya, *Nat. Energy* **2020**, 5, 317.
- [54] A. Knop-Gericke, V. Pfeifer, J. J. Velasco-Velez, T. Jones, R. Arrigo, M. Hävecker, R. Schlögl, *J. Electron Spectrosc. Relat. Phenom.* **2017**, 221, 10.
- [55] M. Salmeron, *Top. Catal.* **2018**, 61, 2044.
- [56] M. Favaro, F. Abdi, E. Crumlin, Z. Liu, R. van de Krol, D. Starr, *Surfaces* **2019**, 2, 78.
- [57] R. Kortlever, J. Shen, K. J. P. Schouten, F. Calle-Vallejo, M. T. M. Koper, *J. Phys. Chem. Lett.* **2015**, 6, 4073.

- [58] J. P. Perdew, K. Burke, M. Ernzerhof, *Phys. Rev. Lett.* **1996**, 77, 3865.
- [59] N. Saunders, A. P. Miodownik, *Bull. Alloy Phase Diagrams* **1990**, 11, 278.
- [60] S. Fürtauer, D. Li, D. Cupid, H. Flandorfer, *Intermetallics* **2013**, 34, 142.
- [61] G. Wulff, *Z. Kristallogr. – Cryst. Mater.* **1901**, 34, 449.
- [62] Y. Duan, *Phys. Rev. B: Condens. Matter Mater. Phys.* **2008**, 77, 045332.
- [63] W. Ren, X. Tan, J. Qu, S. Li, J. Li, X. Liu, S. P. Ringer, J. M. Cairney, K. Wang, S. C. Smith, C. Zhao, *Nat. Commun.* **2021**, 12, 1449.
- [64] A. Bagger, W. Ju, A. S. Varela, P. Strasser, J. Rossmeisl, *ChemPhysChem* **2017**, 18, 3266.
- [65] B. H. Frazer, B. Gilbert, B. R. Sonderegger, G. De Stasio, *Surf. Sci.* **2003**, 537, 161.
- [66] M. Álvarez-Moreno, C. de Graaf, N. López, F. Maseras, J. M. Poblet, C. Bo, *J. Chem. Inf. Model.* **2015**, 55, 95.